Setup and Calibration of a Suite of State-of-the Art Microrheology Techniques

A thesis presented in partial fulfilment of the requirements for the degree of
Master of Science in Physics
at Massey University, Palmerston North, New Zealand

Bradley William Mansel

2011

ABSTRACT

Microrheology is the study of the flow and deformation of fluids on the micrometre scale. It has many benefits over the use of traditional rheomoeters to measure the mechanical properties of fluids. Microrheology has small sample sizes, can extract information about the underlying heterogeneities, often has a lower setup cost, can measure to higher frequencies and can measure the viscoelasticity of in-vivo samples. Work has been carried out to setup and calibrate four different microrheology techniques, namely: diffusing wave spectroscopy, dynamic light scattering, multiple particle tracking and probe laser tracking with a quadrant photodiode and optical traps. This resulted in the ability to measure the viscoelastic properties of a material over approximately eight orders of magnitude, with nanometre resolution on the most sensitive technique; diffusing wave spectroscopy. The link between free Brownian motion and a particle diffusing in a harmonic potential was used to calibrate the trap strength of the optical tweezers, enabling a comparison of three different trap calibration techniques. Calibration of the trap strength in optical tweezers resulted in a good agreement between different methods, although, the power spectral density method proved easier to implement and more accurate over the range of laser powers, making it the superior method to use. To illustrate the power of microrheology techniques, the mechanical properties of standard viscous and viscoelastic fluids were first compared. Also organelles in pollen tubes were tracked to simply and accurately measure properties of a complex biological system in-vivo.

ACKNOWLEDGEMENTS

There would be no way that this would have been possible without the help of many people! So here we go!

Bill Williams, it has been awesome having you as a supervisor, your never ending enthusiasm, encouragement and knowledge has made this a great experience! So cheers Bill!!! Oh and thanks for all those beers and food in Wellington, I didn't forget.

Steven Keen (aka Meaty) I learned a huge amount about optical tweezers and working in the lab in general, thanks so much for that!

Philip Patty, your help with the light scattering experiments was awesome; I really learned a lot from you, many thanks!

Lisa Kent, thank- you for the help with the DNA and pollen tubes, hopefully the DNA will be stretched soon.

Yacine Hemar, thank-you for originally setting up the DWS, it's still going strong; we have only slightly modified it.

Erich Schuster, cheers for thesis racing dude, well done for winning!

Mum and Dad (Baldrick), thank-you for all the support and encouragement in my studies it has been greatly appreciated!

Matt, thanks for help with the pollen tube work.

The rest of Bill's group you have been great to work with, cheers guys!

Thank-you to all my friends and family for the support, a special thanks to James (aka J Billo) and the Wells and Young's Brewing Company for the Thursday night Crest, Palmy would not be the same without discussing the world at large over a beer reviewed by drinkpedia.org as: Imagine war, pestilence, famine and death abjectly tossed into a blender with a pint of sour milk. Imagine all the worst things in the world mixed with the dregs from a septic tank and you still wouldn't come close to understanding how gut-wrenchingly vile Crest actually is. Simply put, it is the most disgusting beer I have ever tasted in my entire life.

CONTENTS

TABLE OF FIGURES

1 INTRODUCTION

Mechanical properties of materials play a vast role in everyday life, from mayonnaise that will not easily flow from your sandwich, to the paint on the walls of your house, which dried without running to create a smooth finish [1]. Traditionally to quantify the mechanical properties of a fluid one must use an expensive bulk rheometer that requires a large amount of sample and is limited in the range of measurements by its own inertia. In this thesis recently developed techniques to measure the mechanical properties of materials on the micro scale are directly compared. These techniques known as microrheology can measure to much higher frequencies, use a smaller sample volume, extract information about how homogenous a sample is and often are much less expensive to setup than a bulk rheometer. There are many interesting applications for microrheology in biological studies: as these techniques exert very low forces and the sample volumes used are very small it is common to study tissue in- or ex- vivo. Studies such as measuring properties of the extracellular matrix or diffusion in the intestinal mucus of live Trichosurus vulpecula tissue, are two examples of the abundance of experiments currently being undertaken using microrheology in the Institute of Fundamental Sciences at Massey University.

2 THEORY

2.1 RHEOLOGY

Rheology is the study of the deformation and flow of matter. Matter can be rheologically classified using two different values, elasticity and viscosity. A simple solid displays a purely elastic response to stress, in that energy is stored. A simple fluid displays a purely viscous response to stress where all the energy is dissipated. A complex fluid displays both a viscous and elastic response to stress, called viscoelastic [1, 2].

Viscosity is colloquially described as the property of a fluid that contains information on how easily the fluid flows. A more rigorous definition is the dynamic shear viscosity, η, defined as: the ratio of the shear stress exerted on a surface, the shear stress, σ, to the rate at which the shear changes, the shear rate, $\dot{\gamma}$ [1]. Giving:

$$\eta = \frac{\sigma}{\dot{\gamma}} \tag{1}$$

Commonly, a mechanical rheometer applies a small amplitude oscillatory shear strain to a fluid, $\gamma(t) = \gamma_0 \sin(\omega t)$ where γ_0 is the amplitude and ω is the frequency of

oscillation, and measures the shear stress [1, 3]. The shear strain, γ, is also defined as the time integral of the shear rate. If the strain amplitude is small so that the fluid structure is not significantly deformed and the material remains in equilibrium, the time dependent stress is linearly proportional to the strain, giving[1]:

$$\sigma(t) = \gamma_0[G'(\omega)\sin(\omega t) + G''(\omega)\cos(\omega t)] \quad (2)$$

$G'(\omega)$ is the response in phase with the applied strain, called the storage or elastic modulus, which describes the energy stored in the system when the strain is applied. $G''(\omega)$ is the response out of phase with the applied strain, called the loss or viscous modulus, this describes the energy dissipated in the fluid when the strain is applied [1, 3]. The complex shear modulus is defined as:

$$G^* = G' + iG'' \quad (3)$$

2.2 MICRORHEOLOGY

Microrheology studies the storage and dissipation of energy in soft matter at the micrometre or sub-micrometre scale. It has the ability to probe the complex viscoelastic response of materials revealing the underlying complex structure. Furthermore microrheology can probe the local heterogeneity of a material revealing greater information about the structure of the complex material of interest [4].

Microrheology relies on measuring the position of localized micron sized probe particles. Motions of the probe particles, either mechanically driven (active microrheology) or undertaking Brownian motion due to thermal energy from the environment (passive microrheology), provide viscoelastic information from the Hertz to the megahertz regime. The focus of this thesis is purely passive microrheology.

There are numerous advantages to microrheology techniques to measure viscoelastic properties of materials. The required sample volumes for microrheology are in the order of microliters, while traditional rheometers require millilitre volumes. This makes microrheology ideal for costly or rare materials. Microrheology applies very small strains making it ideal for fragile materials. A bulk rheometer has a limited range of frequencies, limited by the inertia of the tool [2, 3, 5].

Microrheology is a relatively new method that has recently been shown to reproduce traditional rheological experiments, in many materials, to very high accuracy [5]. The main difficulty with microrheology has been calculating the storage and loss moduli. Recent work by Mason has enabled a method that tolerates noise in the data compared

to other methods involving the inverse Laplace transform and power spectrum density [6].

Many microrheology techniques are well characterised, although there is little information on what is achievable with current advances in instrumentation. This thesis investigates the limits of speed and accuracy achievable with current advances in instrumentation, such as state-of-the-art correlators and cameras, by directly comparing different methodologies and equipment.

To obtain the storage and loss moduli of the complex material of interest the mean square displacement (MSD) of the tracer particles must first be measured, defined in three dimensions as:

$$\langle r^2\,(\tau)\rangle = \langle [\mathrm{x(t+\tau) - x(t)}]^2 + [y(t+\tau) - y(t)]^2 + [z(t+\tau) - z(t)]^2 \rangle \tag{4}$$

Where, τ, is the lag time, t, is the time value and x, and y, represent position data. The MSD is measured in either 2 or 3 dimensions, depending on the technique: if the material is isotropic then the 2 dimensional MSD can be scaled to give a 3 dimensional result. There are a number of experimental techniques to measure the MSD, each with its own advantages. The MSD shows the response of the tracer particle to the applied stress, either from thermal motion or applied driving force. If a material is purely viscous (a simple fluid), the MSD of the tracer particle will increase linearly with time, on a logarithmic plot having a slope of one, as shown in figure (1). While a purely elastic material (a solid), will have no increase in the MSD with time [5]. These are the two limiting cases; many materials of interest are viscoelastic, having a slope on a logarithmic plot of MSD versus time between zero and one. Additionally materials often display differing viscoelastic properties at different time scales.

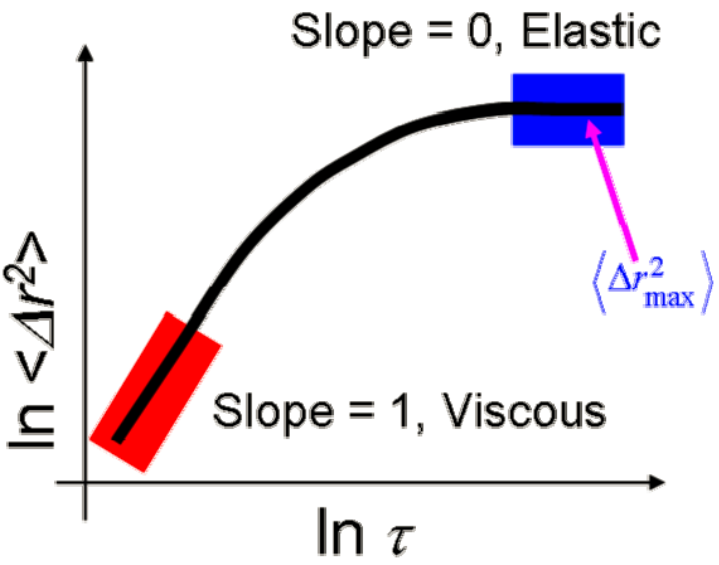

Figure 1: Extract from: Dasgupta, 2004 , sketch showing the MSD of a viscoelastic medium.

Tracer particles embedded in a **purely viscous medium** have a MSD defined by:

$$< r^2\ (\tau) >= 2dD\tau \tag{5}$$

Where τ is the lag time, d is the dimension and D is the diffusion coefficient. Diffusion in a purely viscous material is defined by the ratio of thermal energy to the drag friction coefficient, which can be:

$$D = \frac{k_B T}{f} \tag{6}$$

Here, T, is the temperature and f is the drag friction coefficient which for added spherical tracers can be calculated by Stokes drag equation for a sphere with low Reynolds number [7]:

$$f = 6\,\pi\eta\,a \tag{7}$$

Here, η, is the viscosity of the material and a, the radius of the tracer particle(s). Once the slope of the MSD verse lag time is obtained, by performing a linear fit over a range of lag times, the viscosity can be extracted using equations (5-7).

Tracer particles embedded in a **viscoelastic medium** do not have such a simple relation between the MSD and diffusion. However, a Generalised Stokes-Einstein

relation can be used, accommodating a frequency dependent viscoelasticity of a complex fluid:

$$\tilde{G}(s) = \frac{k_B T}{\pi a s \langle \tilde{r}^2(s) \rangle} \tag{8}$$

In the above equation $\langle \tilde{r}^2(s) \rangle$ is the Laplace transform of the MSD and, $\tilde{G}(s)$ is the viscoelastic spectrum as a function of Laplace frequency, s [4]. This gives a method to quantify the rheological properties of a viscoelastic medium and calculate the storage and loss modulus from the MSD measurement. Many methods are available to implement this scheme, although Mason and Weitz's numerical method is possibly the most popular method, due to its ability to handle noise and simplicity [6].

First the MSD plot is fitted to a local power law. The logarithmic differential is then calculated:

$$\alpha(\tau) = \frac{d \ln \langle \Delta r^2(\tau) \rangle}{d \ln(\tau)} \tag{9}$$

The logarithmic differential is used with, Γ, the gamma function in the algebraic form of the GSER:

$$|G^*| \approx \frac{k_B T}{\pi a \langle \Delta r^2(\tau = 1/\omega) \rangle \Gamma[1 + \alpha(\tau = 1/\omega)]} \tag{10}$$

Now defining δ as:

$$\delta(w) = \frac{\pi}{2} \frac{d \ln |G^*(\omega)|}{d \ln \omega} \tag{11}$$

We obtain the storage and loss moduli with respect to frequency:

$$G'(\omega) = |G^*(\omega)| \cos(\delta(\omega)) \tag{12}$$

$$G''(\omega) = |G^*(\omega)| \sin(\delta(\omega)) \tag{13}$$

In this thesis four different techniques were used to measure the positions of micron sized particles embedded in soft materials, namely: Dynamic Light scattering (DLS), Diffusing wave spectroscopy (DWS), multiple particle tracking (MPT), and probe laser tracking with a Quadrant Photo Diode (QPD) and optical traps. The different techniques and methods were optimized to improve both speed and accuracy, and the results compared. Figure (2) shows a plot of the frequencies obtainable using different techniques.

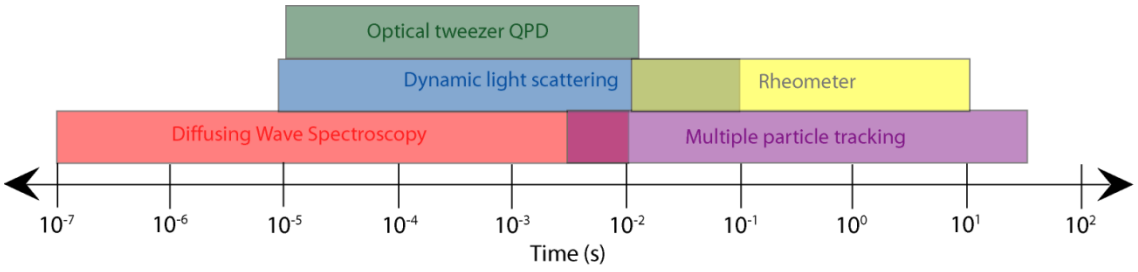

Figure 2: Plot showing the frequency range accessible using different techniques.

3 TECHNIQUES

3.1 DYNAMIC LIGHT SCATTERING

Light scattering techniques for microrheology use a coherent mono chromatic light source and detection optics to measure the intensity of light scattered from tracer particles of a known size, embedded in a material of unknown viscoelastic properties [2]. This differs from traditional sizing techniques, where the viscosity is known but the particle size unknown. Light emitted from the sample produces a dynamic speckle pattern, resulting from the interference of light of different phases. The phase differences are due to a difference in path length of scattered light. By measuring the intensity fluctuations of one speckle, at a single spatial position, information about the diffusion of particles in the sample can be gathered [8]. By calculating the correlation function of light intensity fluctuations as a function of lag time, the MSD of the scattering particles can be calculated. The faster the particles are diffusing through the sample, the faster the correlation function decays [5]. The correlation function is defined by:

$$g^{(2)}(\tau) = \frac{\langle I(t)I(t+\tau)\rangle}{\langle I(t)\rangle^2} \tag{14}$$

Here, τ, represents the lag time, t, the time and the angular bracket denotes a time average [8].

For ergodic samples the auto correlation function can be simply converted to the field auto correlation function, $g^{(1)}$, using the Siegert relation [5]:

$$g^{(2)}(\tau) = 1 + \beta\left|g^{(1)}(\tau)\right|^2 \tag{15}$$

The coherence factor, β, is related to the experimental setup, and for a properly aligned system using an optical fibre for the collection of light, should be close to unity [5].

For an ergodic sample the time averaged intensity is equal to the ensemble average intensity [5].

Dynamic light scattering (DLS) uses a sample containing a low number of scatterers to ensure the light emitted from the sample is scattered only a single time [5].

Central to DLS experiments is the scattering vector, q, defined by:

$$q = \frac{4n\pi}{\lambda} \sin\left(\frac{\theta}{2}\right) \tag{16}$$

Where, λ, represents the wavelength of the incident laser light, n, the refractive index of the medium surrounding the sample and, θ, the angle the incident beam makes with the detector [5].

This section covers work by Dasgupta 2004, for more information see reference [5] or earlier work by Pecora [8]. The scattering vector has units of inverse length and this length defines on what length scale motion of the scatterer can be observed [5]. The motion of probe particle(s) on this length scale results in a change of path length of the scattered light by one wavelength, causing a maximum change in intensity of the scattered light. The choice of scattering angle is more complex than it might appear and is dealt with in the optimisation section. Ultimately, for traditional DLS experiments, the q vector must be known to extract information about the displacements made by the particles [5]. If the light is scattered a second time information is still present, although encoded with multiple scattering events. Recently develop techniques such as; multiple scattering suppression, by the Schurtenberger group [9] can extract this information, although it is not common as in many cases sample optimisation provides a simpler solution.

3.1.1 Experimental Setup

Light emitted from a continuous wave, vertically polarized, laser is directed through the sample held in a goniometer. Detection optics in the form of a gradient index optics lens, single mode optical fibre splitter, two photo multiplier tubes and correlator are interfaced to a computer and convert fluctuations in the scattered light into a correlation function signal. The goniometer has a bath surrounding the sample and is filled with a fluid of a similar refractive index to the curvette, to help eliminate light reflections from the surface of the curvette, as well as providing angular control. A polarized laser combined with a crossed polarizer on the detection optics helps to reduce the chance of light that has not been scattered entering the detection optics, which helps improve the signal. Two Photo multiplier tubes are used to calculate the

cross correlation function, as opposed to an auto correlation function, to help circumvent dead time in the electronics as well as helping eliminate after-pulsing effects [5]. The effects of after-pulsing can be seen in figure (7) and a schematic of the experimental setup shown in figure (3).

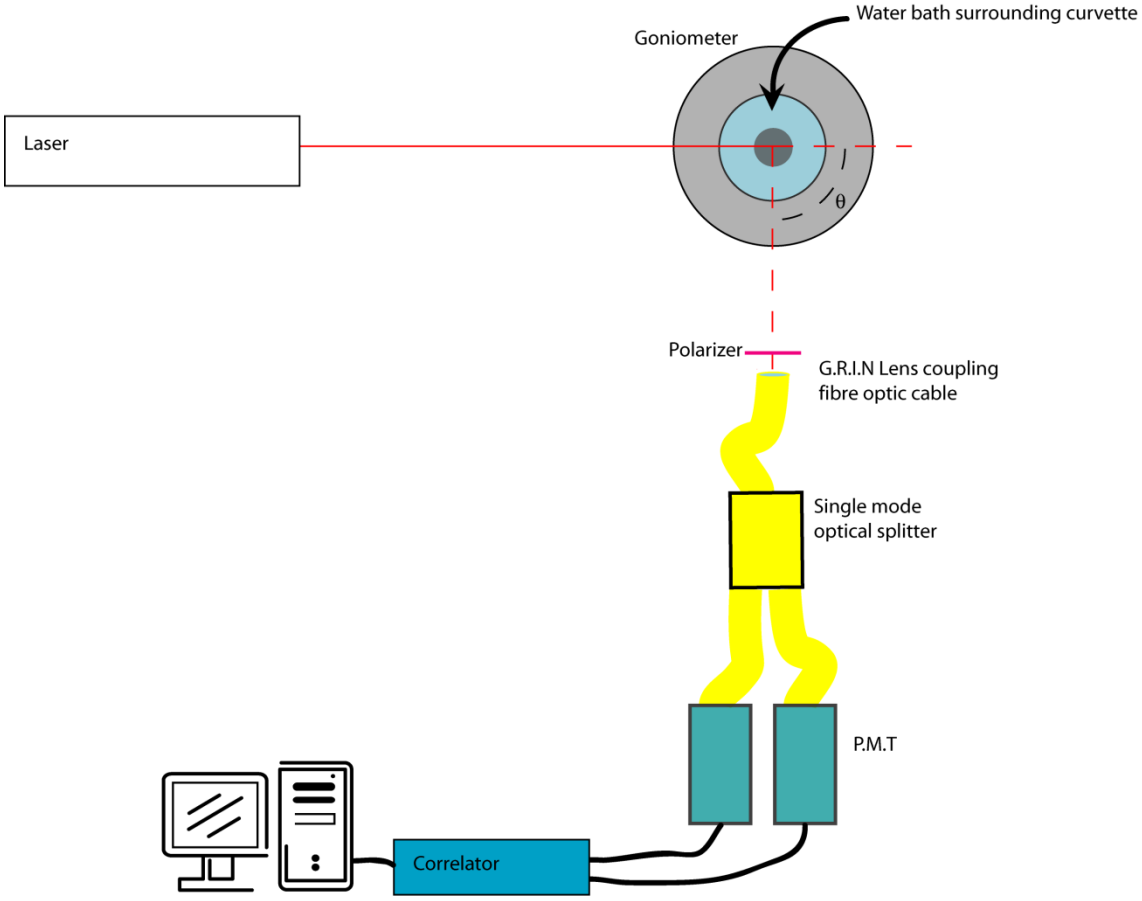

Figure 3: Schematic of DLS apparatus used.

3.1.2 Extracting the MSD from correlation data

In DLS, where single scattering events dominate, the decay of the field correlation function, $g^{(1)}$, is related to the diffusion of the particles in the sample by:

$$g^{(1)}(\tau, q) = e^{-Dq^2\tau} \tag{17}$$

Here, τ, represents the lag time, q, the scattering vector and, D, the diffusion coefficient which, by equation (5) can be written as [8]:

$$g^{(1)}(\tau, q) = e^{\frac{-q^2\langle \Delta r^2(\tau)\rangle}{6}} \tag{18}$$

$\langle \Delta r^2(\tau)\rangle$ represents the MSD. By inverting this equation one obtains the MSD versus lag time from the field correlation function.

3.2 Diffusing Wave Spectroscopy

At high frequencies DLS is limited by the sensitivity of the correlator. This limitation can be overcome by adding many scatterers to the sample. The light now diffuses through the sample taking a random walk of length, l, the mean free path [10]. The diffusion of light through the sample means that if each individual scatterer was to move a very small amount, the overall path that the light travels is changed very dramatically, resulting in a much higher sensitivity than DLS. To make measurements in materials with a very large number of scatterers a statistical approach must be used to derive the form of correlation function [10]. To ensure the accuracy of the statistical approach the number of scatterers must be large enough to make the direction of light from the sample completely random [10]. Light scattering in the high scattering limit is known as diffusing wave spectroscopy (DWS).

There exist two fundamental approximations central to the validity of DWS theory [10]. The first is related to approximating that the light takes a random walk through the sample, this diffusion approximation neglects any interference effects of the light as it travels through the sample and assumes that the light intensity diffuses [10]. The second is how the phase information of the light is treated [10]. An average scattering event is used to approximate the many scattering events in a sample [10]. From the diffusion approximation knowledge of the path length is used to find the number of scattering events that contribute to each path [10].

3.2.1 Experimental Setup

The equipment used for DWS is very similar to that used for DLS. The main difference is that no goniometer is required as there is no angular dependence for DWS in transmission configuration. Another difference is the incident beam is expanded, in our case, to around 8 millimetres to distribute the intensity of the light across the width of the cuvette. A schematic of the experimental setup used can be seen in figure (4)

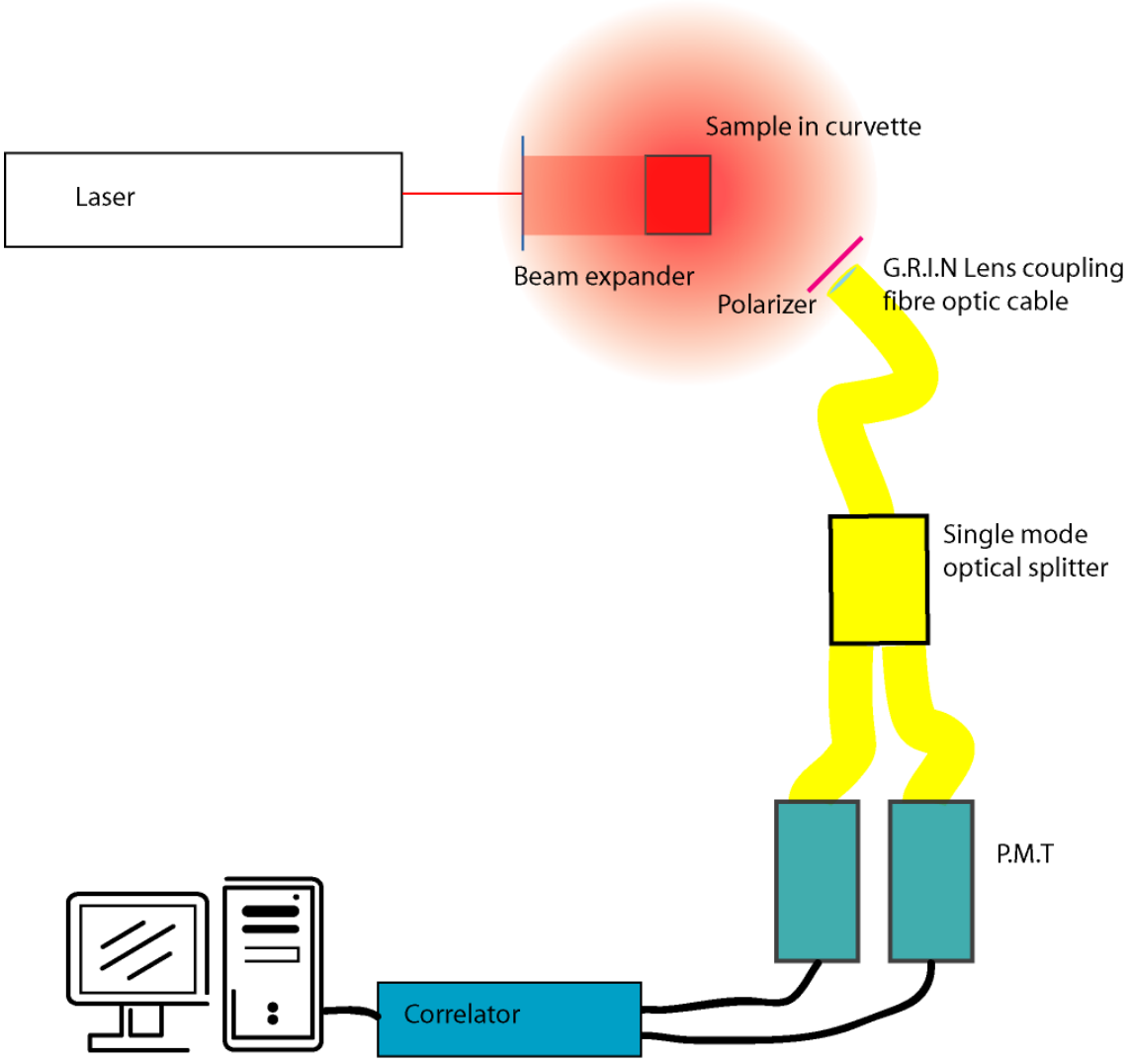

Figure 4: Schematic representing DWS setup.

Light emitted from either a continuous wave, vertically polarized, HeNe or Ar ion laser is expanded to 8mm using a beam expander then scattered by the sample, held in a standard cuvette with a thickness of 4mm. The scattered light is coupled to a single mode optical fibre using a gradient index (GRIN) lens, split by a single mode fibre optic beam splitter and sent to two photo multiplier tubes (PMT). The correlation function is then calculated using a cross correlation method in software on a standard personal computer running the correlator.

The measurement of the length a photon must travel before its direction is completely randomized, l^*, is fundamental to DWS theory as it is needed to extract the MSD from the correlation function, and because it shows if the number of scatterers present in a sample is large enough to randomize the light exiting the sample[11]. By ensuring l^* is at least 4 times smaller than then thickness of the sample one can ensure the light is strongly scattered, producing statistically viable results [11].

3.2.2 *Extracting the MSD from DWS Correlation and Intensity Data*

By comparing the transmitted intensities of a reference sample and unknown sample, T_{ref}, and, T_{unk}, containing the same phase volume of added scatterers, one can calculate the transport mean free path of the unknown sample, l^*_{ref}. The relation between mean free path and transmitted intensity are [5]:

$$T_{ref} \propto \frac{l^*_{ref}/L}{1 + 4l^*_{ref}/3L} \tag{19}$$

$$T_{unk} \propto \frac{l^*_{unk}/L}{1 + 4l^*_{unk}/3L} \tag{20}$$

Here L represents the sample thickness.

Taking a ratio of the two one obtains:

$$l^*_{unk} = \frac{T_{unk}}{T_{ref} + \frac{4l^*_{ref}}{3L}(T_{ref} - T_{unk})} l^*_{ref} \tag{21}$$

To calculate the MSD in transmission geometry, with uniform illumination over the face of the sample, an inversion is performed on the following equation [10]:

$$g^{(1)}(\tau) = \frac{\left(\frac{L/l^* + 4/3}{z_0/l^* + 2/3}\right)\sinh\left(\frac{z_0}{l^*}\sqrt{k_0^2\langle r^2\rangle}\right) + \frac{2}{3}\sqrt{k_0^2\langle r^2\rangle}\cosh\left(\frac{z_0}{l^*}\sqrt{k_0^2\langle r^2\rangle}\right)}{\left(1 + \frac{8t}{3\tau}\right)\sinh\left(\frac{L}{l^*}\sqrt{k_0^2\langle r^2\rangle}\right) + \frac{4}{3}\sqrt{k_0^2\langle r^2\rangle}\cosh\left(\frac{L}{l^*}\sqrt{k_0^2\langle r^2\rangle}\right)} \tag{22}$$

Here, L, represents the thickness of the sample, l^*, the transport mean free path of the medium, the source of diffusing intensity to be distance, z_0, inside the sample. We approximate, z_0, to be equal to l^*. k_0 is the wave vector of the incident light, equal to $2\pi\lambda$ [5, 10]. For a detailed description on the theory of DWS and the mathematics behind equation (22) -see chapter 16 of *Dynamic light scattering: The Method and Some Applications* edited by Wyn Brown, which covers this extensively [10].

3.2.3 *Optimizing Light Scattering Experiments*

Two photomultiplier tubes are used to avoid dead time in the detector electronics and remove after-pulsing effects (figure 7). A photon hitting one of the PMT emits an electron which travels and hits a dynode, emitting more electrons. The electrons then pass through a series of dynodes amplifying a single electron approximately 10^6 times [5]. When a photon hits the cathode of the PMT there is a delay time before another photon can be detected by the PMT. The dead time results from the time it takes an

electron to travel through the PMT, and it is typically a few tens of nanoseconds[5]. By using two correlators in a cross correlation mode one can reduce the dead time of the electronics, as when one PMT is inactive the other PMT can receive a photon [5].

3.2.3.1 Optimization of the Scattering Angle for DLS Experiments

The scattering vector, q, can be maximised by using a larger angle, giving the advantage that the speckle dynamics are faster, resulting in measurements down to smaller time lags [8]. This can be advantageous as interesting rheological properties can be present at shorter lag times, also if DLS is used as a complementary technique to multiple particle tracking then obtaining measurements to shorter lag times will be the goal of DLS. If the scattering angle is deceased then measurements to larger lag times can be obtained, if DLS is used complimentary to a faster technique such as DWS it is advantageous to decease the scattering angle. If the intensity of the light source was infinitely large then the signal to noise would be increased by increasing the scattering angle, by equations 17 and 18 it can be observed that increasing the angle makes the correlation function decay faster [8]. If the correlation function decays faster then there will be a greater number of single correlation functions to average over in a given experiments total duration. Using statistics the signal to noise relating the number of averages that are performed can be written as[8]:

$$\frac{S}{N} = \sqrt{Dq^2\tau T} \tag{23}$$

Here the symbols have their usual meaning and T is the total duration of an experiment. To increase the signal to noise one can increase the intensity of scattered light, as is explained in the section on correlators. The scattering intensity is highly dependent on many factors, the refractive indices of the medium and particle, particle size, incident light power, unwanted scattered light and the scattering angle. First it will be assumed that the power of the incident light is a constant, as in most cases it is sensible to use the highest laser power without damaging the equipment. The scattering of light from dielectric particles can be predicted using Mie theory, which reduces to Rayleigh scattering when the particle size is smaller than $1/10^{th}$ the wavelength of light [12]. The intensity of scattered light from Rayleigh scattering is [12]:

$$I_s = I_0 \frac{1+\cos^2\theta}{2R^2}\left(\frac{2\pi}{\lambda}\right)^4\left(\frac{n^2-1}{n^2+2}\right)\left(\frac{d}{2}\right)^6 \tag{24}$$

Here, I_0 represents the intensity of incident light, θ the scattering angle, R distance between scatterer and detector, λ the wavelength of light, n the refractive index of the particle and d, the diameter of the particle. It can be observed from equation (24) that in the Rayleigh regime the intensity of scattered light depends on the angle by $1 + \cos^2\theta$, making a maximum of scattered intensity when θ, the scattering angle, is 0 or 180 degrees, and 50% intensity when the scattering angle is 90 degrees. Mie theory, for particles approximately the same size or larger than the wavelength of light, has a much more complex relation between the scattering angle and scattering intensity [12]. A simple way to help choose which angles will give you an increase in scattering intensity, for these larger particles, is to use an algorithm for the explicit calculation of Mie scattering, the one shown as an example here, called Mieplot, is a Java based applet available freely on the web (figure 5).

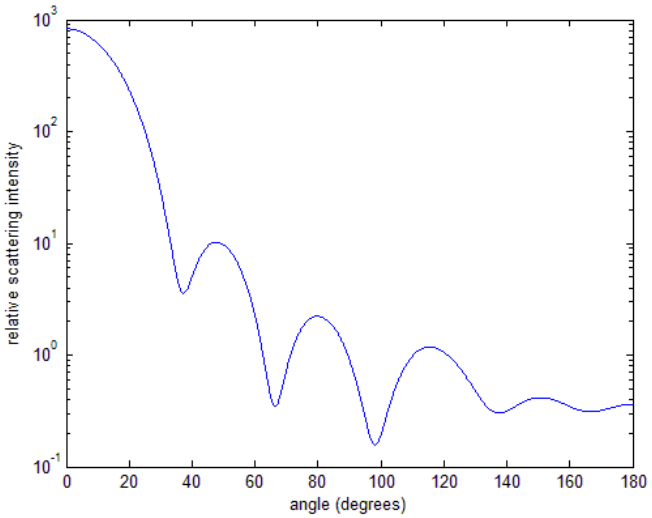

Figure 5: Plot showing the angle dependence of the scattering intensity for a 0.5 micron polystyrene particle immersed in water.

As can be seen on figure 5 in the Mie regime the highest scattering intensities occur at small angles, although at small angles there is also a larger amount of unwanted scattered light. Unwanted scattered light can result from fluctuations in laser intensity, reflections or flare, convection currents in the scattering cell, foreign matter such as: dust, bacteria, air bubbles and heterogeneities due to improper mixing [8].

To find the optimum scattering angle one should decide on the time lags relevant for the dynamics of the system being studied and select an angle based on this. Then starting from this angle one can experimentally view the signal to noise. From this any unwanted scattered light can be reduced by changing the scattering angle slightly, to

move away from any major drops in signal as predicted by Mie theory. If the signal to noise is still unacceptable one can continue to increase the duration of the experiment until a satisfactory signal to noise is obtained to extract the MSD.

3.2.3.2 Correlators

The upper limit on the frequency fluctuations that can be measured using light scattering techniques, to measure rheological properties, is limited by the speed and sensitivity of the correlator. The current smallest delay time that can be measured is 1.56ns using a commercially available correlator, costing ten thousand dollars. Middle of the range correlators, capable of lag times down to approximately 10ns can be purchased for around two thousand dollars. The very short delay times possible with state-of-the-art correlators introduce a different problem, in that the number of photons hitting the detector in this short period of time is very small, resulting in a low signal to noise.

The following section follows work done by Dasgupta 2004, for more information one should read through his work. To increase the signal to noise the experiment can be run for a longer duration or the intensity of the light source increased. If the intensity of the light is increased then Poisson statistics can be used to estimate the error. Error in the measurement is given by: $\sqrt{I}/I = 1/\sqrt{I}$, where I represents the intensity. Although, at very low light levels noise is primarily due to dark counts in the PMT. Dark counts are the result of thermally excited electrons in the PMT that result in an anode current in the absence of incident light. If the experiment is run for a longer period of time the error is again related to Poisson statistics, with the error given by: $1/\sqrt{N}$, here N is the approximate number of independent measurements $N = T/\tau$. T is the total measurement time and τ the characteristic decay time. To ensure a small error the total measurement time must be approximately 1000 times larger than the characteristic decay time. It can be seen from figure (6) that running an experiment for a longer duration will result in a less noisy correlation function at short time lags.

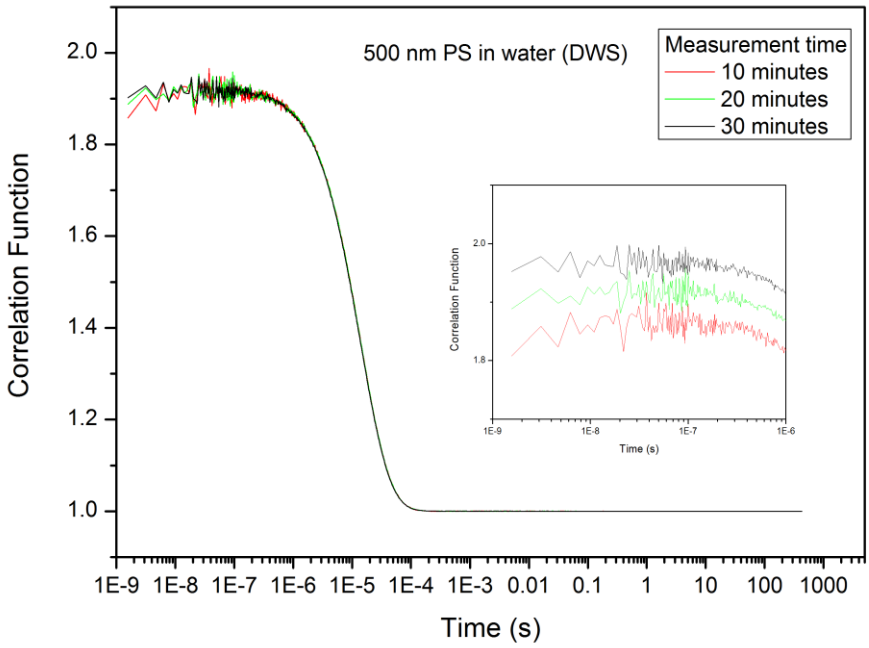

Figure 6: Effects of total measurement time on noise in the correlation function.

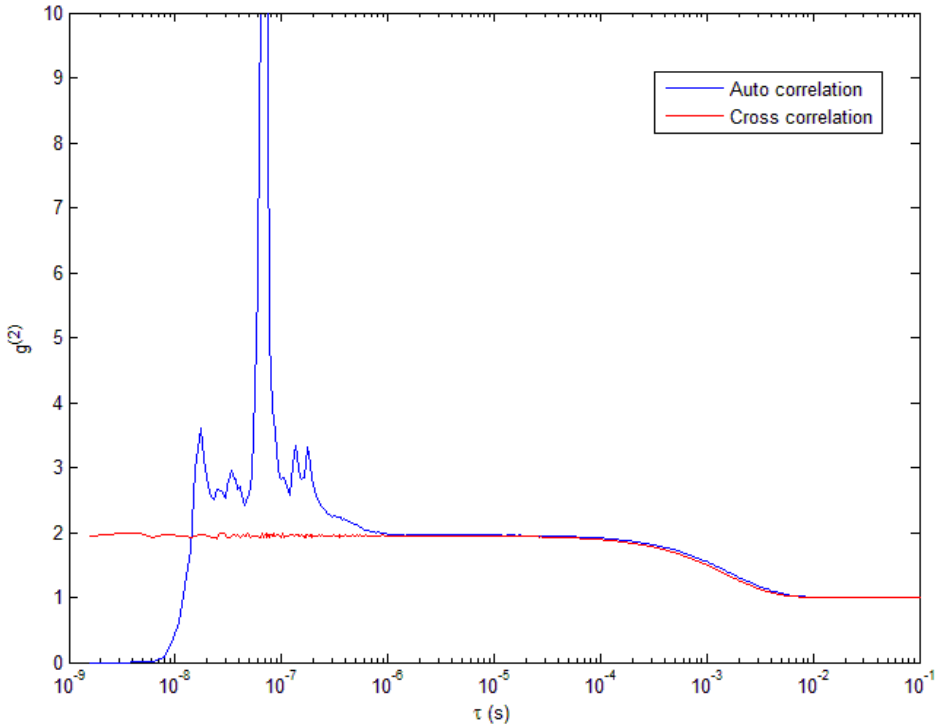

Figure 7: Comparison of cross and auto correlation for DLS of water, 500nm particles. Spikes in the auto correlation data are due to after pulsing effects.

From figure (7) significant after pulsing effects can be seen in the auto correlation data below 1 micro second, it can be seen that using a cross correlation method is especially important for small particles or large scattering angles where the speckle dynamics are faster. From figure (8), a plot of the MSD for 500nm particles in a glycerol water mixture, the difference between a $10,000 (Flex02) and $2,000 (Flex 99) correlator can be seen. It is surprising that the Flex02 correlator achieves a better temporal range in the larger time lags and only marginally better at short time lags and no increase in range for DLS (figure (9)), a rather unexpected result.

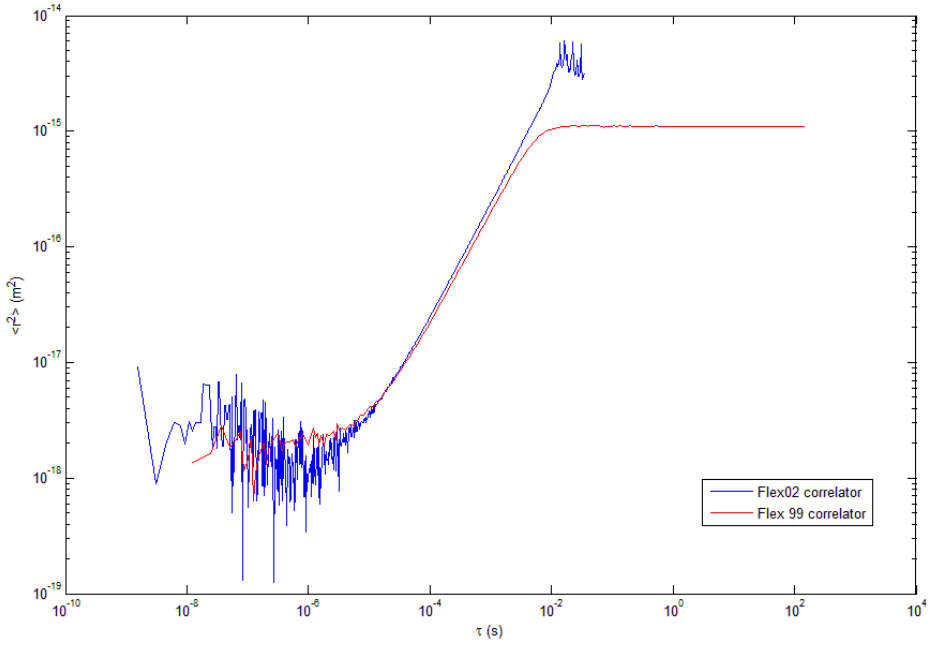

Figure 8: MSD plot for different correlators for diffusing wave spectroscopy.

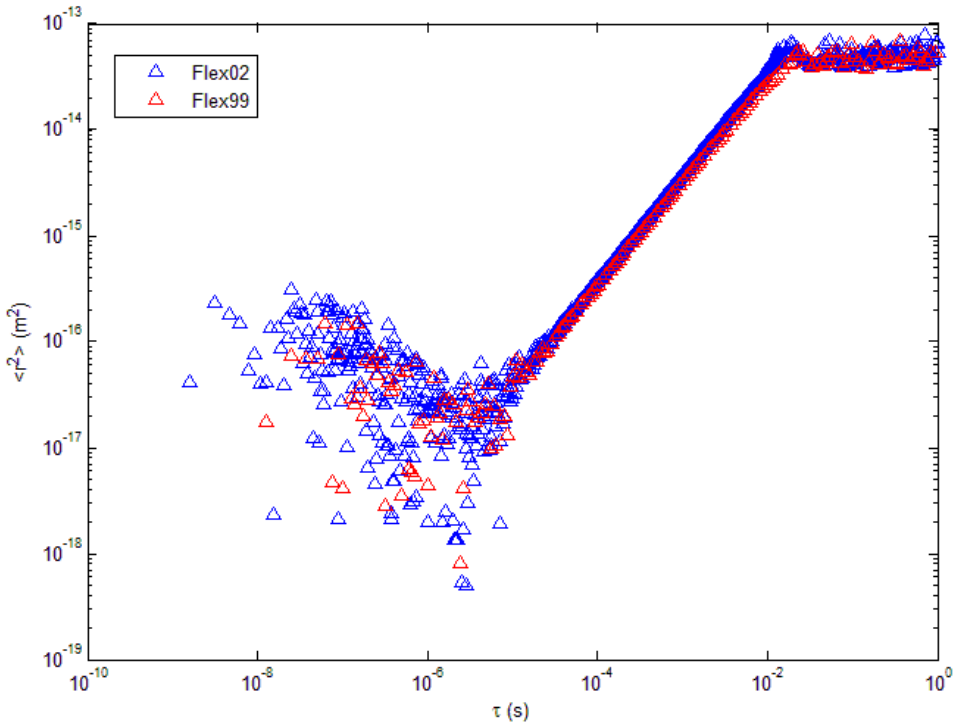

Figure 9: Plot showing effects of different correlator for dynamic light scattering of 500nm polystyrene particles embedded in water. Little difference can be seen between the two correlators.

3.2.4 Advantages and Disadvantages of Light Scattering Techniques

Generally light scattering techniques have the advantage that they have a low setup cost, are well known and produce very reliable results due to the statistical averaging of taking measurements over a long duration of time. They are disadvantaged in that information about the heterogeneity of the sample is difficult to extract, but can be accomplished using techniques modified from the traditional methods, such as multispeckle DWS [13, 14].

3.2.4.1 Dynamic Light Scattering

DLS, one of the more common light scattering techniques, cannot measure to the high frequencies of DWS and also has a slightly higher setup cost as a goniometer is required for angular control. A goniometer is not required for DWS as angular dependence is washed out. Many measurements can be taken and averaged over a period of time during one experiment, allowing DLS to produce very consistent results. If the scattering angle is reduced it is possible to obtain the particle dynamics out to tens of seconds [5].

3.2.4.2 Diffusing Wave Spectroscopy

DWS is a robust, well proven technique. The robustness is in part due to the statistical improvements made by taking the measurements over a long period of time and the many scatters present in a sample. DWS can achieve higher frequency measurements than any other method, due to a small displacement of the bead causing an additive effect in each successive scatter through the sample. Traditional DWS experiments do not however have the ability to extract any information about the homogeneity of the sample, as the scattered light is randomised, although a more modern technique known as multi speckle DWS can be used [13, 14].

3.3 Results: Light Scattering Optimisation

Figure (10) shows that using smaller particles and/or having lower viscosity solutions results in MSD plots moving to smaller time lags. It is also seen that the overall range of displacements measured is slightly larger for water, compared with glycerol. The larger range of displacements that can be measured, for water, is due to the refractive index of water being lower, resulting in a smaller q vector meaning that the correlation function will not decay as fast for water as it does for glycerol. The range of displacements measured using DLS changes when the particle size is changed, in that, smaller displacements can be measured with smaller particles. The two techniques are in good agreement, although the DWS data for glycerol are slightly low compared to DLS, this remained after repeating the measurement, so more work should be undertaken to determine the exact reason for this. One reason could be a slight change in the detection angle of the goniometer; DLS is very sensitive to the angle, with an angle change of only a degree or two having a significant effect on the MSD. Another source of this disparity could be due to polydispersity of the probe particles, resulting from manufacturing defects or clumping of the particles.

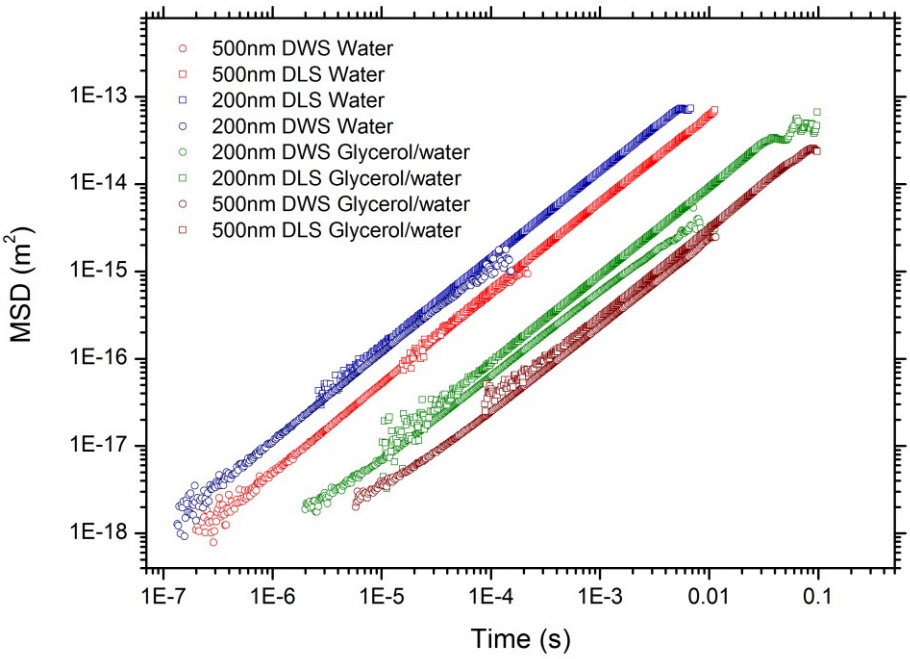

Figure 10: Plot showing particle size and viscosity dependence of the MSD measured using both dynamic light scattering and diffusing wave spectroscopy.

3.4 Multiple Particle Tracking

Multiple particle tracking typically consists of visually tracking tens to hundreds of probe particles embedded in the material to be studied [2]. Commonly, an epifluorescence microscope with a CCD/CMOS camera is used to record an image series of fluorescence tracer particles as they undertake random walks due to thermal energy in the sample. Fluorescence microscopy has many advantages over bright field microscopy; it produces images with the particles represented as bright spots on a dark background, resulting in images that are the easiest to track using many different tracking algorithms, and allows particles smaller than the wave length of light to be tracked, this is usually not possible using other techniques. Also fluorescence microscopy can be used to visualise regions of the sample tagged with a specific fluorphore, then by changing the filter these regions can be filtered out to increase the signal to noise ratio when tracking the probe particles. This is useful in some samples where one must know the region in the sample where the tracking is taking place, due to the viscoelastic properties changing in specific locations. Other microscopy techniques, such as differential interference contrast (DIC) microscopy can also be used. DIC results in an image with a very high resolution, making the most accurate

tracking in live samples or samples where the particles are larger than the wavelength of light [15]. Image series taken from the chosen microscopy technique are then processed using tracking software, turning the images into x-y coordinate data. From this data the MSD can be calculated and rheological information extracted.

3.4.1 Experimental Setup

A typical MPT setup consists of an inverted epifluorescence microscope combined with a CCD/CMOS camera to record an image sequence of the particles motion, a computer to store the image sequence and also run tracking software. A schematic of the microscope used can be seen in section (3.5.3.3) figure (19).

3.4.2 Advantages Disadvantages

MPT, a relatively new technique, is mainly limited by the temporal resolution of the camera, meaning that a lower frequency is accessible, compared with other microrheolgy techniques. MPT has the advantages of measuring information about the spatial homogeneity of the sample, requiring a small sample volume and is minimally invasive, making it one of the few techniques capable of studying the viscoelastic properties of live samples (where naturally occurring particles might be tracked). The combination of optical tweezers and multiple particle tracking techniques allows one to record the displacements of particles in specific regions of the imaging plane, which is especially useful for highly heterogeneous samples containing interfaces between regions of differing viscoelastic properties.

3.4.3 Extracting Information about Spatial Homogeneity

To study the homogeneity of a sample one can plot the probability of displacements of a certain value observed at each time lag for the duration of the experiment [16]. If the sample is homogenous then one would expect a Gaussian function centred on the origin, the full width at half maximum related to the MSD at that time lag. The plotting of the number of times each particular displacement occurs in a given time lag is known as a Van Hove plot, shown for particles diffusing in water in figure (11) [16]. If significant heterogeneities exist then the Van Hove function will begin to display nubs, regions where the number of displacements that occurred is higher than predicted for a homogenous material. The distance the nubs are from the centre of the plot displays information about the size of the heterogeneity. Often heterogeneity is only observed for distinct time lags.

Information about the underlying structure of the sample can also be extracted by observing the MSD, as shown in figure (12), where the structure of the cytoplasm is directly observed. For polymer solutions and gels the mesh size can be directly observed by measuring the MSD using differing particle sizes.

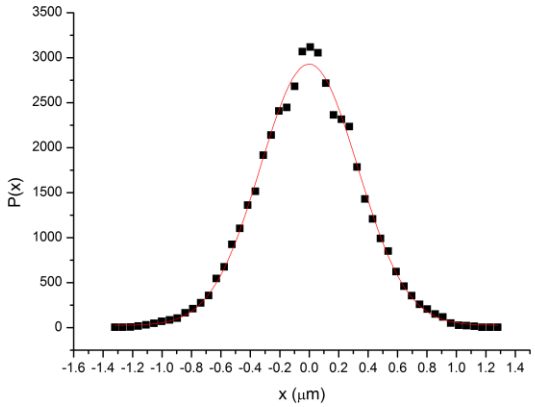

Figure 11: A Van Hove plot of particles in water, a homogenous medium, as can be seen by a good agreement to a Gaussian fit.

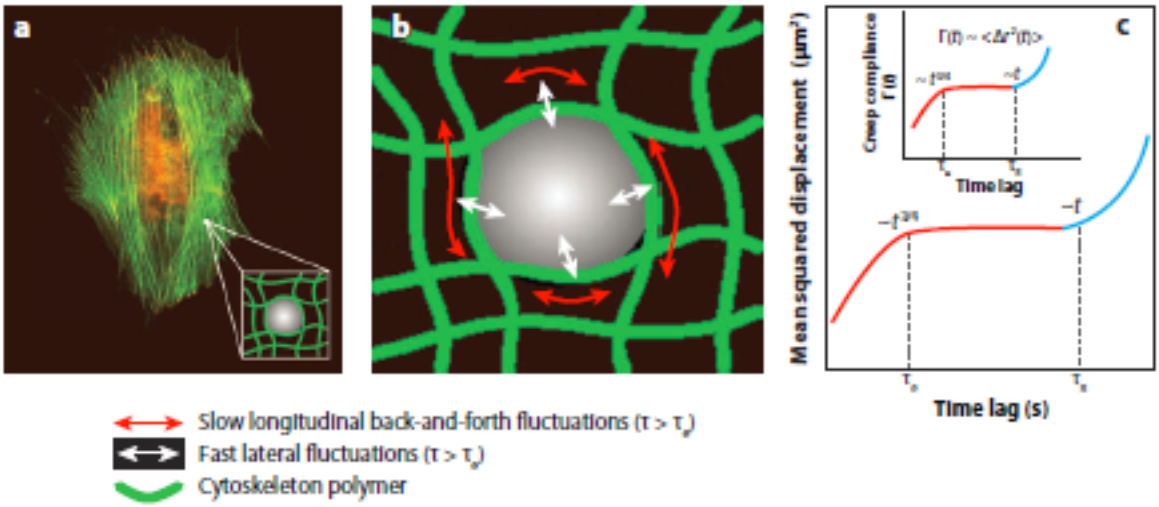

Figure 12: Extract from [17], showing the physical origin of the displacements of particles in the cytoplasm. Here an in vitro cytoskeleton is created using entangled actin filaments, this removes any effects that motor or cross linking proteins. (a) Ballistically injected particles in the cytoplasm, with the particle size much larger than the mesh size. (b) Schematic showing the different displacement of the particle and there relevance to the entangled polymer. At short time lags the bead motion is characterised by the fast lateral bending of the polymer filaments. At median lag times the motion of the particle is a result of the slow lateral motion of the polymer filaments. At the largest time lags the motion of the particles is diffusive as the particles jump from one cage to the next. (c) MSD and creep compliance plots showing the three different regimes of particle motion inside the entangled actin filaments.

3.4.4 Two Point Microrheology Analysis

Microrheology is highly dependent on the interaction between tracer particle and the medium, and effects of the interaction can produce spurious measurements of the viscoelastic properties of the medium [18]. One method to overcome these difficulties is known as two point microrheology (TPM). TPM only differs in the way the data is analysed, in that, rather than just looking at one particle, as was explained in the first section and what will be referred to as one point microrheology (OPM) through this section, TPM measures the cross correlation of pairs of particles [19]. OPM can be thought of as a superposition of the bulk rheology and the rheology of the material at the particle boundary [20]. In many cases TPM measures viscoelastic properties agreeing with those measured using a bulk rheometer, due to the elimination of dependence on particle size, particle shape, and coupling between the particle and the medium [19]. TPM is an intuitive technique, if the two limiting cases of a solid and simple fluid are examined; a solid will exhibit completely correlated motion throughout the sample, while a simple fluid would exhibit very little correlated motion. The median region is quantified by knowledge of the distance between particles, the thermal energy and the cross correlation function [15]. Two point microrheology is very susceptible to any drift or vibration; this appears as completely correlated motion [15]. If the material of interest is homogenous and isotropic on length scales significantly smaller than the probe particle, incompressible and connected to the tracers by uniform no slip boundary conditions over the whole surface, the 2 point and 1 point MSD will be equal[15].

To perform two-point microrheology first the ensemble average tensor product is calculated:

$$D_{\alpha\beta}(r,\tau) = \langle \Delta r_\alpha^i(t,\tau)\Delta r_\beta^j(t,\tau)\delta\left(r - R^{ij}(t)\right)\rangle_{i\neq j,t} \qquad (25)$$

Here i and j label different particles, α and β label different coordinates and R_{ij} is the distance between particles i and j. The distinct MSD can be defined by rescaling the two point correlation tensor by a geometric factor $2r/a$ [15, 19]:

$$\langle \Delta r^2(\tau)\rangle_D = \frac{2r}{a} D_{rr}(r,\tau) \qquad (26)$$

Further information on the mathematics behind the method can be obtained from Crocker 2000 [19], Levine 2002 [20] and Crocker 2007 [15].

A method to remove noise is explained by Crocker 2007 [15]. It is expected that in three dimensions the correlation between particles motion is inversely proportional to the distance separating them. This is due to the fact that larger segments of the material will have slower Brownian dynamics. If the two point correlation function is fitted to the function $\frac{A(\tau)}{r} + B(\tau)$ then the $A(\tau)$ component can be used to compute the two point MSD and rheology, helping to remove any unwanted artefacts from vibration or noise.

3.5 Optimising MPT

To optimise MPT, the camera, microscope and tracking software must all be individually optimised. The camera used for MPT is the central apparatus limiting the temporal and spatial resolution. Current CMOS technology allows the fastest frame rate of any off the shelf camera designed for microscopy [21, 22]. The main problem with this technology is the sensitivity, although these issues are beginning to be addressed [23]. Cameras with a high sensitivity, large detector size, higher speed and small pixel size can obtain a higher amount of information from the sample.

To supply the tracking algorithm with enough information to calculate the position of the particle to sub pixel accuracy, the particle must be represented by at a minimum ~3-4 pixels. The size representation of the fluorescent particles is dependent on the size of the particles, intensity of the excitation fluorescent lamp, the size of each pixel on the sensor and the magnification of the objective lens used. The strength of the fluorescent lamp that can be used is ultimately limited by the speed at which it photo bleaches the fluorophore. One possible method to overcome the photo bleaching difficulties is to use quantum dots, as quantum dots do not photo bleach on the time scales that MPT experiments are carried out.

A limiting factor in achieving a high signal to noise is the amount of background fluorescence. A simple way to reduce the background fluorescence is to create sample chamber with a shallow depth. One way to achieve this is using lab tape to stick two edges of a coverslip to a glass slide, in effect creating a microfluidic channel. A small drop of the liquid of interest can be placed at one of the open ends of the channel; capillary force then sucks the fluid through the channel. To eliminate evaporative drift the ends of the channel must be sealed, this can be accomplished using nail varnish. For best results the glass must be very clean.

3.5.1 Tracking Software

A plethora of different programs and more specifically algorithms exist to track objects in successive images. Both commercial and freeware programs exist. Commercial

software, image pro plus, can track images straight out of the box with little fuss, although it is difficult to alter the tracking parameters and costs around 3000 dollars. One can also write their own program to cater to their own needs, using a very specific algorithm. Kindly people have made free software available that works as well as many commercial packages. There exist four main algorithms, centre of mass, correlation, Gaussian fit and polynomial fit with Gaussian weight.

Particle tracking algorthims implemented in programs ready to use are available on the following web pages:

http://www.physics.emory.edu/~weeks/idl/ This web page is a great resource with links to many different programs written in many different programming languages.

http://physics.georgetown.edu/matlab/ This code uses the centroid algorithm for sub pixel tracking, it is the code used for the majority of the particle tracking in this thesis. Some knowledge of programming in MATLAB is needed to implement the code as it is not a finished program, it is only the tracking algorithms.

http://www.physics.mcgill.ca/~kilfoil/downloads.html A very good resource where code is available for calculating the MSD, two point microrheology and many other useful programs implemented in MATLAB®.

http://www.mosaic.ethz.ch/Downloads/ParticleTracker This page has links to a 2D and 3D particle tracking as published in [24]. The code is implemented using imageJ a popular java based open source image processing and analysis program.

http://personalpages.manchester.ac.uk/staff/david.kenwright/polyparticletracker.html Polyparticle tracker uses a polynomial fit with Gaussian weight, a very powerful tracking algorithm with a good graphical user interface and easy to implement. Details of the algorithm can be viewed in the following publication [25]

The following sections, on the different algorithms, follows work done by Cheezum 2001 [26].

3.5.1.1 Centre of Mass Tracking

The centre of mass (COM) tracking algorithm is used for sub pixel accuracy. It is most commonly used in conjunction with another algorithm, such as correlation tracking,

which locates the position of the particles to pixel level accuracy. COM tracking, one of the computationally simple and efficient algorithms, compares the centre of mass of a particle in two successive images:

$$C_x = \sum_{i=1}^{n}\sum_{j=1}^{m}\left(x_i \cdot \boldsymbol{I_{ij}}\right) \Big/ \sum_{i=1}^{n}\sum_{j=1}^{m} \boldsymbol{I_{ij}} \tag{27}$$

x_i is the coordinate of the pixel in the x axis and $\boldsymbol{I_{ij}}$ is the intensity of that pixel. C_x is calculated for one image and subtracted from C_x for a subsequent image. $\boldsymbol{I}$ is a matrix of intensities that contain both the object and the pixels around the object up to a mask. The mask is used to separate the many beads in one image.

The main disadvantage of this algorithm is when the signal to noise drops below approximately 3 the algorithm starts to calculate the centre of mass of the image not the particle represented by a bright spot on the image[26] (this can also be seen from figure (14), obtained from [26]). It is also susceptible to noise causing the particle shape to deform. This is due to how the algorithm detects the presence of a particle. It does this by the intensity value of the pixels representing the particle i.e. if a pixel is above the threshold value then it is part of a particle. If a pixel on the edge of a particle is over the threshold due to noise then the COM algorithm will calculate an erroneous value, leading to small fluctuations in the measured position. Before this algorithm can be implemented the particle positions must be estimated using a different particle tracking algorithm.

3.5.1.2 Correlation

Correlation tracking does not result in sub pixel accuracy; commonly it is used to find the position of particles to pixel level accuracy, preceding a sub pixel algorithm. Correlation tracking is more computationally taxing than the other methods, although it is more accurate in low signal to noise situations than COM tracking. It calculates the position of the particle by comparing an image to a kernel of a successive image. The kernel, $\boldsymbol{K}$, is then shifted in one pixel increments. For each increment a correlation value is calculated. At the shift where the correlation value is a maximum, the image and kernel are most similar.

$$\boldsymbol{X_{x,y}} = \sum_{i}^{n-1}\sum_{j}^{m-1} \boldsymbol{I}_{x+i,y+j}\left\{\boldsymbol{K}_{i,j}\right\} \tag{28}$$

Here $\boldsymbol{X}$ is the correlation matrix, i, represents pixel location in the x dimension, j, the pixel location in the y dimension and, $\boldsymbol{K}$, the kernel which is a segment of an image consisting entirely of a particle, figure (13) shows the relation between the image, kernel and correlation function. One kernel is used for the entire video.

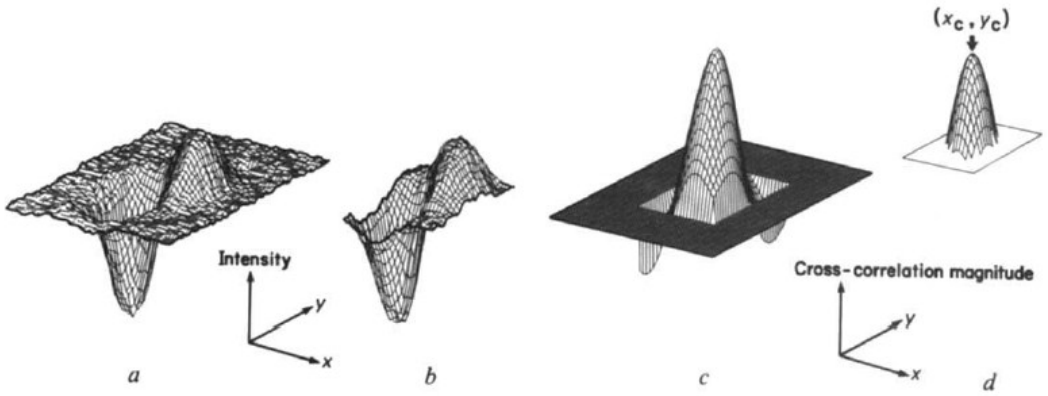

Figure 13: (a) A 3 dimensional plot of the intensity and position of pixels in an image. (b) A plot of the kernel. (c) The cross correlation of the image and kernel. (d) Centroid calculation. Obtained from: [27]

3.5.1.3 Gaussian Fit

Gaussian fitting algorithms result in sub- pixel accuracy when used with a particle represented by a sufficient number of pixels. Gaussian fitting is implemented by fitting a Gaussian curve to the intensity profile of a point source. This algorithm has a low computational intensity and works in low signal to noise situations. Although, this algorithm has the major downfall; that it only works for fluorescent particles or particles represented as a point source. As the intensity profile of the light emitted from the particle must fit to a Gaussian function. The algorithm is represented by the following equation:

$$G(x,y) = A \cdot \exp\left[\frac{(x-x_0)^2 + (y-y_0)^2}{B}\right] \tag{29}$$

Here, x_0, is the x coordinate of the centre of the cure and, y_0, the y coordinate of the centre of the curve. A and B are constants that are allowed to float. Using least squares fitting the values of x_0 and y_0 are found.

3.5.1.4 Polynomial Fitting with Gaussian Weight

This section covers work by; Rodgers 2007, for a more in depth description see reference [25]. Polynomial fitting with Gaussian weight is a newer technique that has the same advantages of the Gaussian fit method while overcoming some of the drawbacks. A polynomial function of 4th order is fitted to the intensity profile of a particles estimated position in the image. The fit is then weighted by a Gaussian function centred on the particle. The centre of the particle is located from the maxima of the polynomial fit. This method enables the tracking of non-spherical objects on a complicated background, while being computationally efficient [25].

$$I_{fit}(x,y) = \sum_{i=0,j=0}^{i+j=4} P_{ij} x^i y^j \tag{30}$$

The intensity map of the image, $\boldsymbol{I}$, is fitted with the above quartic polynomial function. Where x and y denote pixel coordinates. The fit is given a weight at each pixel by the Gaussian function:

$$W(x,y) = \exp\left(-\alpha \frac{x^2 + y^2}{R^2}\right) \tag{31}$$

α, the decay constant, is set to 1 to ensure that the particle itself is weighted and the surroundings are excluded and, R, the estimated particle radius.

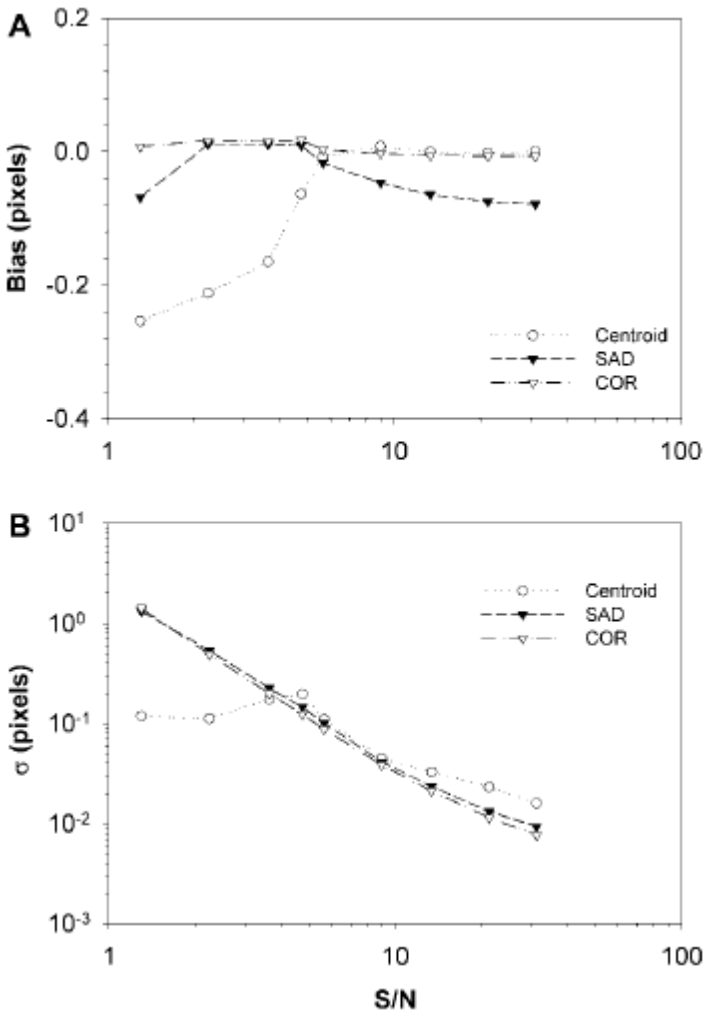

Figure 14: (A) Bias versus signal to noise for a 5 micron target, showing centroid and cross correlation (COR). (B) Standard deviation versus signal to noise. Extracted from Cheezum 2001 [26].

Algorithm	$S/N_{0.1\ bias}$	$S/N_{1.0\ \sigma}$
Gaussian fit	4.2	4.0
Centroid	7.8	6.6
Cross Correlation	4.2	6.3

Table 1: Approximate S/N at which bias and standard deviation drop below 0.1 and 1 pixels, respectively, for various algorithms. Extracted from Cheezum 2001 [26].

Theoretically it can be seen that the different tracking algorithms play a large role in multiple particle tracking experiments. In reality the differences in tracking algorithm can be overcome by optimizing the experimental setup, this can be seen from figure

(14) where at a high signal to noise the different tracking algorithms produce very similar bias and standard deviation. The lower limit where differences in the algorithms become important is a signal to noise of around 4, as can be seen from table (1). A signal to noise of 4 corresponds to approximately imaging single fluorescent molecules. The fluorescent micro spheres imaged for multiple particle tracking are many tens of times brighter than the background fluorescence, providing a high signal to noise. Modern CMOS cameras such as the Hamamatsu orca flash 2.8 have a photo detector array consisting of many megapixels. This results in a particle diameter in the order of tens of pixels, meaning that effects from noise on the edge of a particle have very little effect. Oscillation and drift in an experimental setup create large sources of error and often are the hardest errors to remove.

3.5.2 Error Analysis

Errors in particle tracking can be placed in 4 different categories: Random error, systematic error, dynamic error and sample drift. This will be covered in the following 4 sections. The following sections describe work from Crocker 2007, more information can be obtained from this paper [15].

3.5.2.1 Random Error

Random errors result from camera (or shot) noise. This noise is not a result of camera design; it is a result of the discrete nature of light. This is the probability that the photon will hit the exact spot on the detector. In reality the photon has a probability of hitting any place on the detector, although we know there is a spot where it is most likely to hit and areas of decreasing probability away from this point. We can compute the standard error from statistics:

$$\sigma_x = \sigma_y = \frac{a}{\sqrt{N}} \tag{32}$$

Here σ_x and σ_y is the standard error in the x and y dimension respectively, a is the standard deviation and N the number of photons. This shows that to make a measurement as accurate as possible the most number of photons achieves this. Although a camera is limited in how many photons it can accept before the image becomes saturated. In reality the probe particles position is spread over many pixels on the detector, resulting in a much more accurate measure of the particle position than this statistical analysis represents.

3.5.2.2 Systematic Error

Systematic errors result from improper image pixilation and masking. For instance if the particles are represented by too few pixels the centroid of the particle is rounded to the nearest pixel.

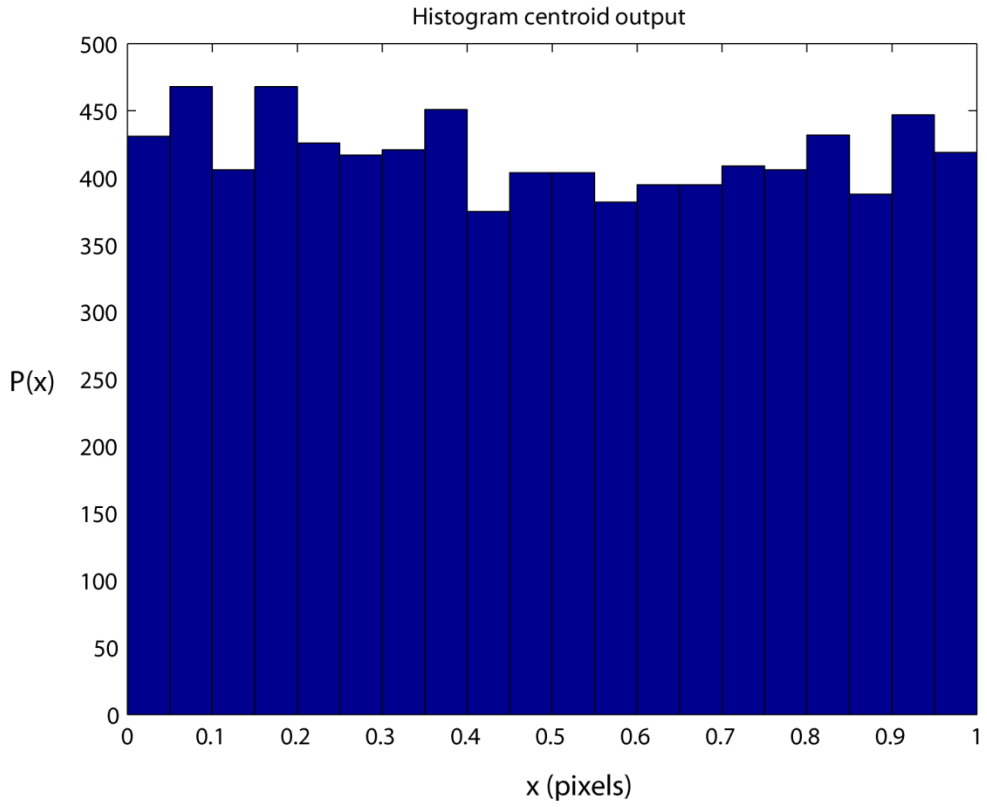

Figure 15: Histogram output of the sub pixel centroid algorithm. No significant pixel bias is shown as the plot is overall flat.

This is known as pixel bias, it can be observed by plotting a histogram of the centroid output. If enough frames and/or particles are present in the image sequence then the centroid output should have an equal probability of every value being represented, resulting in a flat histogram plot (figure 15). Any pixel bias is represented as a sloping plot. Many tracking algorithms use a mask to help remove any effects of other particles or background fluorescence. If the mask is specified to be too small then pixel bias will also result. To check that the mask is correct one should output the mask and detected particles for the first few particles, when a new sample is run, this can be seen in figure (16)

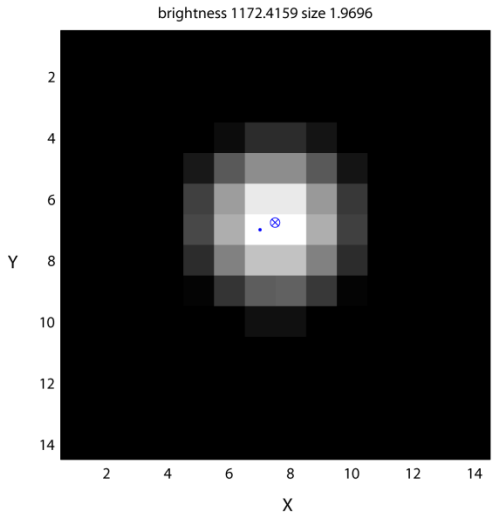

Figure 16: Output from centroid tracking, plotted in pixels to check that the mask size is correct and to ensure artefacts are not being tracked.

3.5.2.3 Dynamic Error

Dynamic errors in measuring the particles displacements are due to systematic underestimation of tracer motion when finite exposure times are used [28]. If a particle moves significantly during the camera exposure, then the measured centroid is a time-averaged position during the exposure. A brighter image can be used to minimise the random error described above, and the easiest way to create a brighter image is to increase the exposure time. However increasing the exposure time also increases the dynamic error. This creates a trade-off where one must have the brightest image possible (longest exposure) while not introducing random error. This can be observed as what appears as super diffusive Brownian motion at short time lags. Crocker 2007 reports that if the mean square motion during the exposure interval is less than a quarter of the mean squared motion between exposures, then the underestimation of the MSD caused by dynamic error will be less than 10%. Although it should be mentioned that this method requires extrapolating the MSD down to time lags shorter

than can be measured using MPT, and also if the material of interest displays significant elasticity then the exposure time needs to be much smaller than a quarter of the frame interval. Using light scattering or quadrant photodiode measurement methods and comparing results one can easily ascertain if the MSD being measured contains significant dynamic or other error.

3.5.2.4 Sample Drift

Drift in a sample or the stage can introduce a large error in measurements. This can result from localised heating in a sample, evaporation from not sealing the cover glass, thermal expansion or mechanical relaxation of the stage. By plotting the x and y particle coordinates verses time, as in figure (17) (for many particles, in the x dimension), one can easily ascertain if the data contains significant drift in either dimension. Some experiments are plagued by significant drift; this may be due to a small air bubble close to the imaging plane traveling up through the sample.

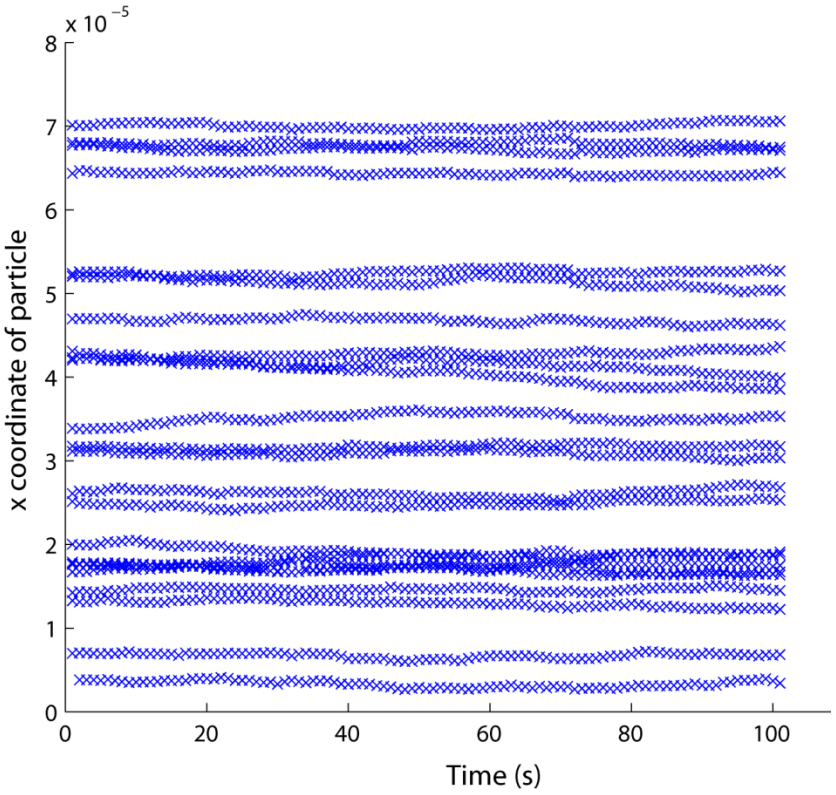

Figure 17: A plot of particle x position verses time, this gives a simple check for large scale drift and oscillations.

A precise method to estimate the static and dynamic errors present in particle tracking is given by Savin and Doyle 2005 [28]. Further work on statistical effects of MPT are covered in Savin and Doyle 2007 [29]. As multiple experimental techniques were used

in the experiments carried out during this thesis, then any significant errors in the MPT data would be revealed.

3.5.3 Optimising Experimental Setup for Microscope Based Experiments

A well optimised experimental setup is essential in any microscope based experiment. Mechanical vibration, present in all buildings, resulting from both external traffic and movement inside the building, has a large effect on measurements at the micro meter scale. To eliminate mechanical vibration, the microscope must be mechanically isolated. This can be achieved through the use of an air damped table. Any device with moving parts especially fans must be removed from the mechanically isolated table. Air currents also have a large effect on measurements at this scale. Fans present in air conditioning units as well as cooling in computers and other electronic devices will produce vibration in your system. Having the operator sitting too close to the setup will create drift due to their body heat causing thermal expansion of the stage [15]. This can be minimised by moving the operator further from the microscope and/or installing a curtain around the microscope [15].

3.5.3.1 Cameras

A charged couple device (CCD) is an array of photodiodes that produce a different charge for different amounts of light hitting a sensor[30]. For a CCD this charge is transported to one corner of the chip, where an analogue to digital converter turns each pixels charge into an 8 bit binary number, for black and white images [30]. While complementary metal oxide semiconductor (CMOS) image sensors also use an array of photodiodes to convert photons into electrons, they differ in the way they convert the charge into a signal[31]. CMOS image sensors have several transistors next to each pixel, to convert the charge into a digital signal. This means that many of the photons hitting the sensor miss a pixel, causing a drop in sensitivity. CMOS cameras are able to achieve a higher temporal resolution than CCD cameras as they are not limited in the speed that charge can be moved from one site to another[31]. CMOS sensors achieve this by having individually accessible cells.

Other factors contributing to the accuracy of camera are the size of the pixel sensors. Smaller pixel sensors produce a higher quality image. The overall size of the detector and the number of pixels both produce a higher quality image if increased.

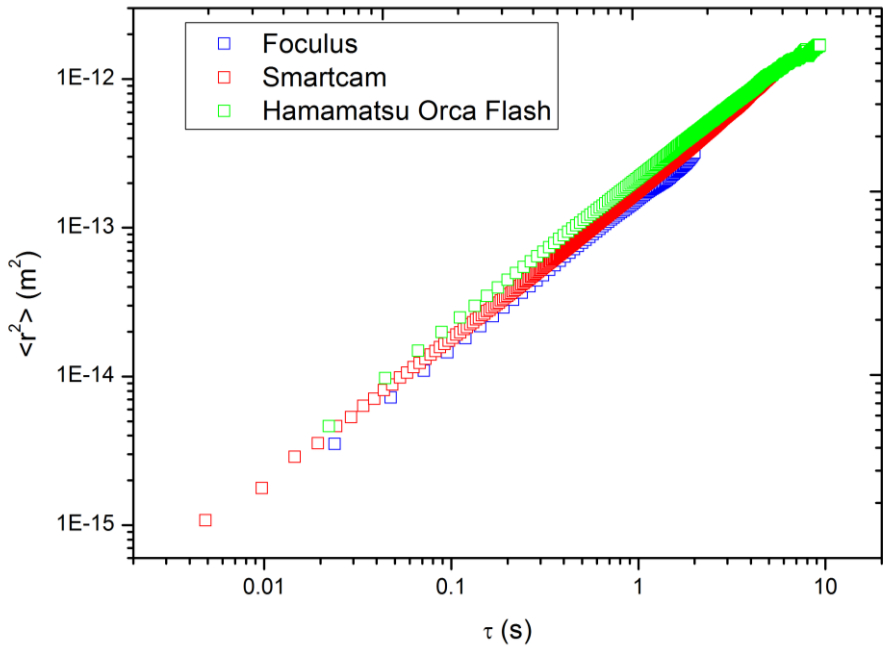

Figure 18: Comparison of different cameras, for further information on the specifications refer to the Appendix.

3.5.3.2 Magnification

For high signal to noise applications, it is advantageous to have the highest possible magnification. The highest possible magnification results in the particles being represented by the maximum number of pixels, enhancing the accuracy of the tracking algorithm [32]. However as the magnification is increased the illumination of each pixel decreases as the square of the magnification. This results in a decrease in the signal to noise proportional to the magnification, if the illumination is not increased [32] and therefore for low signal to noise applications, the highest possible magnification will not always result in the best image sequence for tracking. As a result one must take care in selecting the correct magnification objective lens. A simple method to check that the selected objective is of the correct magnification before running an experiment is to record a single image, then using an image analysis program such as ImageJ (http://rsbweb.nih.gov/ij/), to find the brightness of an individual pixel on a particle. This can then be compared to the background brightness on the image. By comparing the two intensity values one can roughly estimate the signal to noise. If the signal to noise is too low (< ~10) then a lower power objective lens can be chosen. As most microscopes are only equipped with approximately 4 objective lenses, this basic method will suffice to quickly give an indication of what objective is appropriate for the sample. A lower magnification objective will also result in a larger field of view in the

sample, thus, more individual particles positions can be measured, and resulting in better statistics of the ensemble averaged MSD.

3.5.3.3 Numerical Aperture

A high numerical aperture (NA) objective lens creates a higher resolution image than the equivalent lower NA objective lens [32]. This would suggest that a high NA objective lens would create a superior image for tracking, although, a high NA objective also results in a small point-spread function, meaning a smaller image [32]. In reality these two competing effects relating to the NA lens used cancel out. A calculation by Carter et al 2005 shows that if the signal to noise is high (around 30) then there is no effect on the NA used. Another example in Carter et al 2005 is an experiment performed using different tracking algorithms and comparing data for a 0.6 NA and 1.3 NA lens. This showed no relation between the NA and accuracy of tracking.

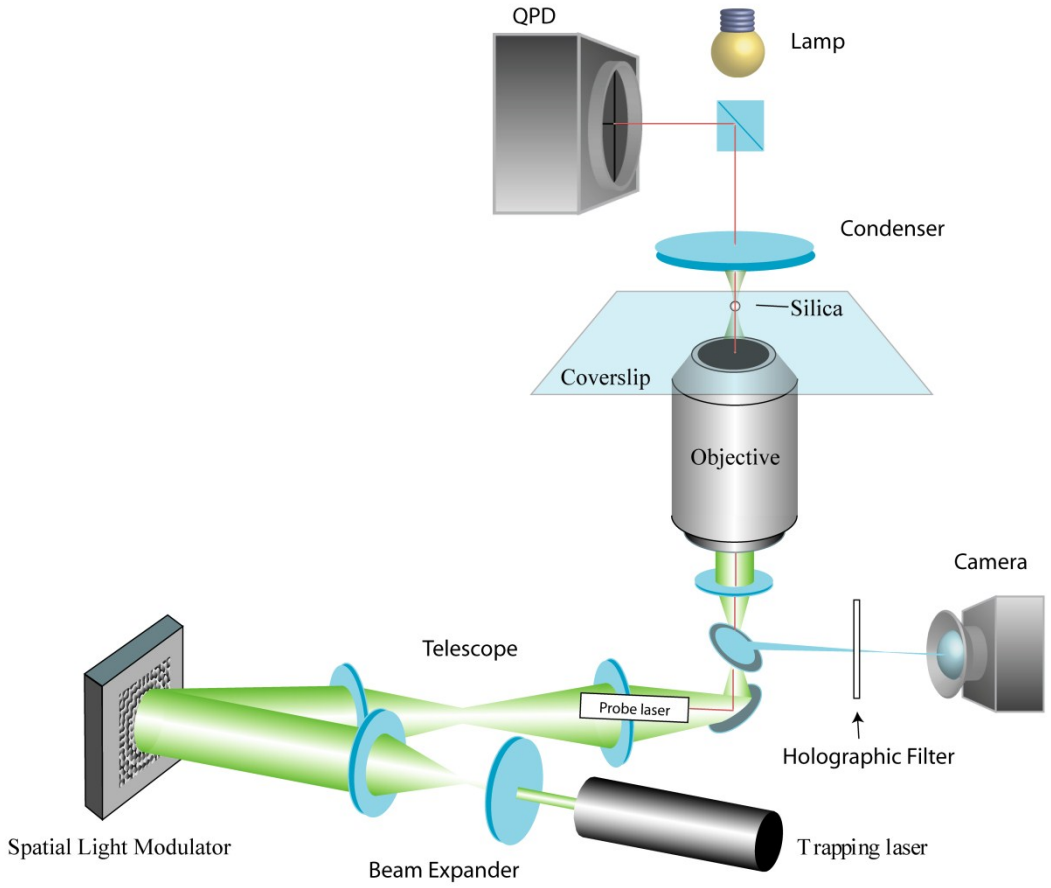

Figure 19: Schematic of the microscope and optical tweezers apparatus. Image sourced from Stephen Keen and modified.

3.5.3.4 Allan Variance for Drift Optimization of a Microscope

If no drift is present in an experimental setup, a very unlikely situation, then the longer the experiment is run the better the accuracy of the measurement. If drift is present, as in nearly every experimental setup, running the experiment for the longest duration will not result in the highest accuracy measurement, it will actually result in a worse measurement than if the measurement was taken for a shorter duration. One can check the optimum time length to record an experiment by using the Allan Variance. Defined as:

$$\sigma_x^2(\tau) = \frac{1}{2}\langle (x_{i+1} - x_i)^2 \rangle_\tau \tag{33}$$

We define τ as the time lag, $x_i$is the mean over the time interval defined as $\tau = f_{acq}m$, where m is the number of elements in that interval; the angle brackets denote arithmetic mean [33]. The Allan variance is only valid for particles trapped in a purely viscous fluid or adhered to the coverslip (this is due to the frequency dependence of a viscoelastic material). Most commonly the Allan variance is used on optical tweezers apparatus, the tracking performed using a QPD, although with modern CMOS cameras approaching the kilo Hertz regime one could optimise particle tracking experiments in this way. One can think of the Allan variance as a statistical evaluation of your experimental setup, the general trends of the Allan Variance can be seen in figure (18). The Allan variance decreases as the number of measurements (number of lag times evaluated) increases, although it increases for any low frequency deviations. Resulting in a minimum where there are enough measurements to make the data statistically viable but not at such long lag times that drift will be having a significant effect on the measurement.

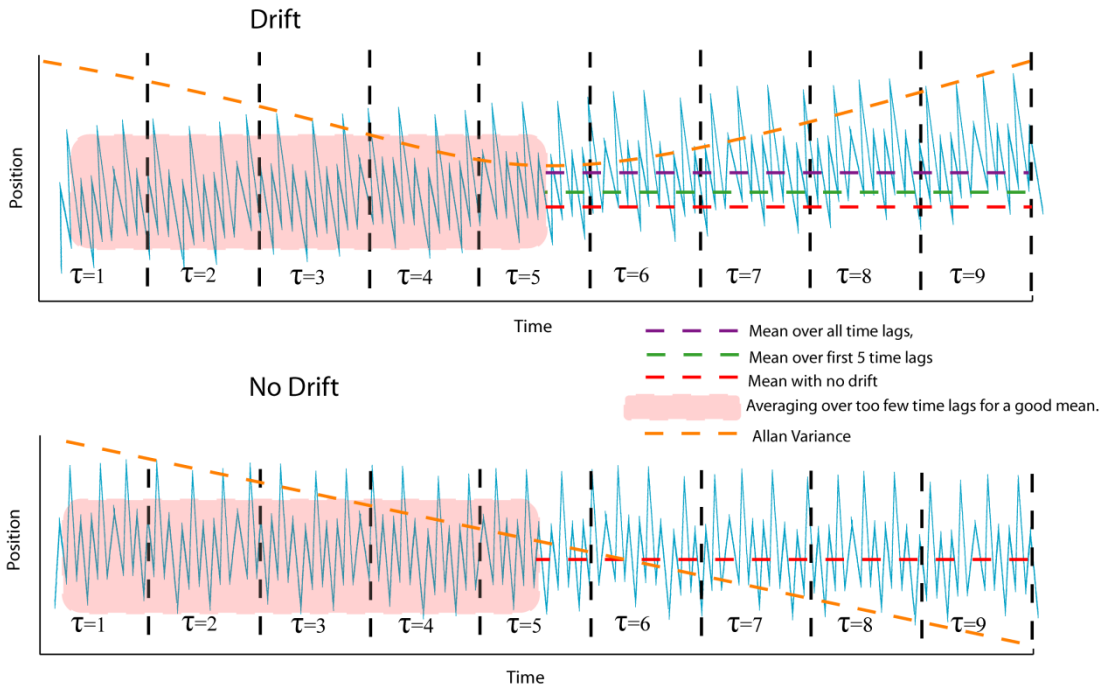

Figure 20: Schematic showing the relation between a particles mean position and the Allan Variance. It can be seen that in a perfect experiment, with no drift, the Allan variance decreases for the duration of the experiment, but where drift is present the Allan variance has a minimum corresponding to when the effects of sampling statistics and drift are balancing out.

Examples of the Allan variance for an optically trapped particle and a particle stuck to the cover slip are shown in figures (21) and (22), it can be seen that the Allan variance for a trapped particle has a minimum at much longer times than the one for a particle stuck to the cover slip. This is due to the stability of the trapping laser, it is very isolated from noise and drift. The water around trapped particle also acts as “suspension” removing drift that the stage undertakes, as long as the trapped particle is far from the coverslip. The particle stuck to the coverslip shows how much the stage moves, this is very difficult to remove from the setup.

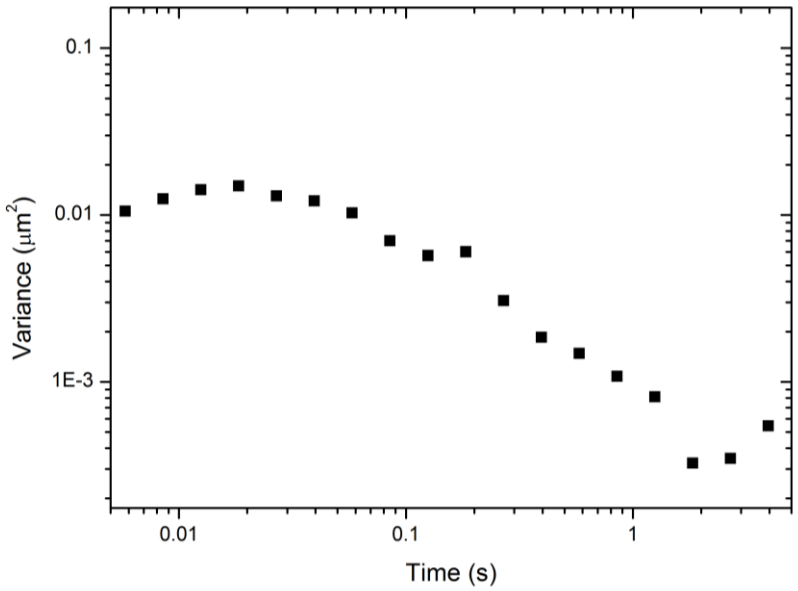

Figure 21: The Allan variance for an optically trapped particle. A minimum can be seen at approximately 2 seconds corresponding to the optimum time duration to run an experiment.

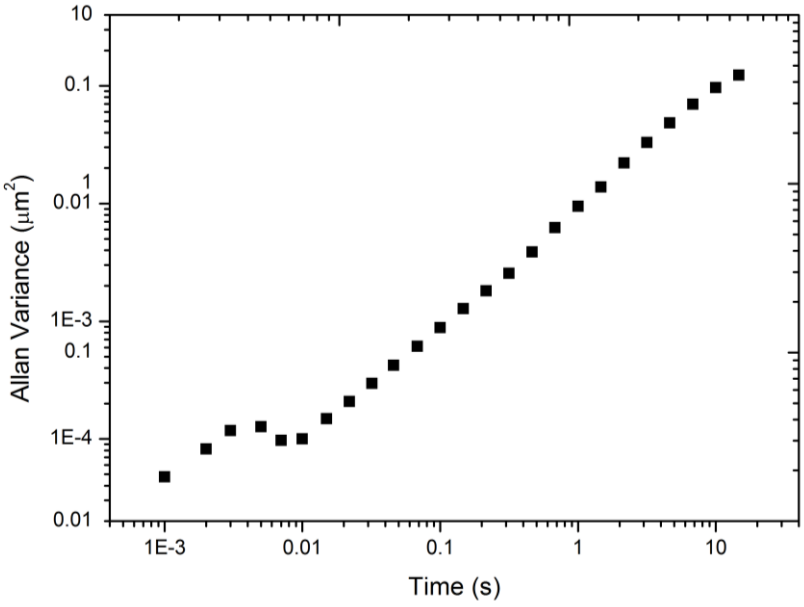

Figure 22: Allan variance for a particle electrostatically adhered to the cover slip. The large amount of drift present in the stage is revealed by the minimum being at approximately 0.01 seconds compared to 2 seconds for an optically trapped particle.

3.5.3.5 Power Spectral Density to Locate Sources of Vibration

To help locate sources of vibration one can plot the power spectral density (PSD) of a particle either electrostatically adhered to the coverslip or trapped in an optical trap. Any sources of vibration will appear as an irregular spike in the PSD. The PSD, as explained in [34], is defined as:

$$P_k = \frac{|\tilde{x}_k|^2}{T_{msr}} \tag{34}$$

Where, $\tilde{x}_k$, is defined as:

$$\tilde{x}_k = \int_{-T_{msr}}^{T_{msr}} \mathrm{d}t e^{i2\pi f_k t}\, x(t) \tag{35}$$

The position, $x(t)$, has been measured for time, T_{msr}, and $f_{k=k/T_{msr}}$, where k is an integer.

Adding a small amount of sodium chloride to a silica bead and water solution causes the silica beads to electrostatically adhere to the coverslip. Tracking the motion of the stuck beads enables one to directly measure any drift or vibration present in the stage. Figure (23) shows the PSD of a particle in an optical trap, the plateau shows the effect of the trap, if the trap strength is increased the plateau extends out to higher frequencies. Figure (24) shows the PSD for a particle adhered to the coverslip, the particle is still undertaking some motion, diffusing in two dimensions, which is represented by the sloping plot. No large spikes, representing vibration, in either PSD plot can be seen, indicating good mechanical isolation of the microscope.

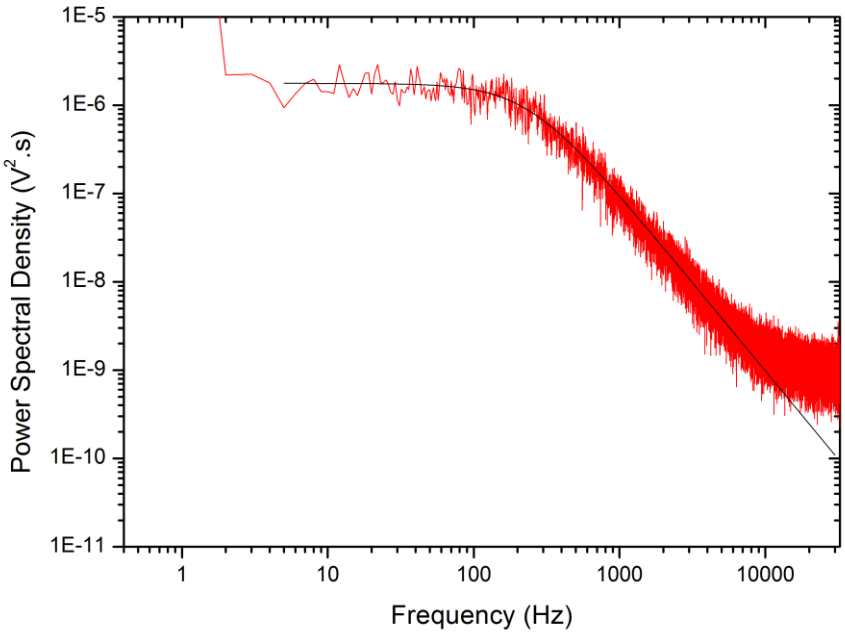

Figure 23: The PSD for a 1.86 micron silica particle held using an optical trap in water. The black line shows a good fit to a Lorentzian, as expected for a trapped particle. Measured using a quadrant photodiode (QPD). The plateau, that can be seen around 10,000 Hz, is most likely due to resolution limit of the QPD. Inertial effects would only be expected at frequencies greater than around 100,000 Hz.

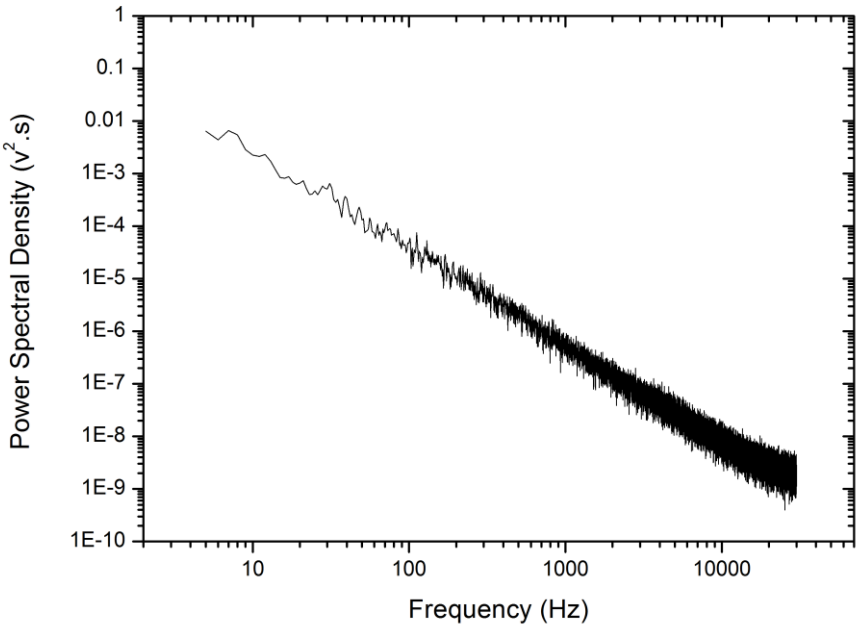

Figure 24: The PSD for a 1.86 micron silica particle electrostatically adhered to the coverslip. PSD measured using a QPD. No distinct spikes in the signal can be seen, indicating good mechanical isolation of the microscope.

3.6 QPD Measurements Using Optical Traps

Individual particles can also be tracked using a laser and QPD. A quadrant photodiode (QPD) is a photodiode that is divided into four segments. For tracking particle displacements a laser is used to scatter light from a particle and produce an interference pattern on the QPD. Any movement of the interference pattern on the QPD is related to a change in output of the QPD and therefore if a particle is located between the laser and QPD then any motion of the particle will result in a change in the output of the QPD. A QPD produces an output in volts and a calibration factor must be measured to relate the voltage to a displacement. Although this creates an extra step when making measurements, as compared to real space tracking, a QPD is advantaged as the data volume is low so measurements into the hundred Kilo Hertz frequency regime are possible.

However a QPD is limited in the maximum displacement it can measure and as particles are diffusing in 3 dimensions it is essential to keep the particle in the range of the QPD so measurements can be undertaken. Optical tweezers use a tightly focused laser to hold and manipulate micron sized particles [35], this can be utilised to hold a particle in the detection region of the QPD/laser apparatus (figure 20).

The radiation pressure that light exerts on dielectric particles has been known about for many hundreds of years, from the observation that a comets' tail always points away from the sun [36]. It has taken until the 1970's for technology to advance far enough so that it is possible to routinely manipulate particles using light [37]. The aptly named optical tweezers have become a stable part of the bio-physicists quiver of experimental techniques. Optical tweezers allow the exertion of very small forces, in the Pico Newton regime, to micron sized dielectric particles [35].

The central apparatus to an optical tweezers set-up is a microscope, most commonly an inverted model [3]. This provides two main functions, visualisation of the (sub)micron sized particles and focusing the laser light at the imaging plane through the use of a high numerical aperture lens [38]. A high numerical aperture lens is necessary to provide a gradient force, which tends to pull the particle towards the focus, larger than the scattering force, which pushes the particle away from the focus [39]. The optical tweezer setup used is known as holographic optical tweezers, and employs a spatial light modulator (SLM), differing from other more simple setups that use a steerable mirror. A SLM provides the ability to make multiple steerable traps and move objects in the z-axis using a single laser, in real time [40, 41]. The SLM functions by creating a manipulable complex interference pattern, this results in regions of high laser light intensity at the imaging plane to form multiple traps [42]. Data acquisition can be performed either using a CCD/CMOS camera or a quadrant photo diode (QPD). Data recorded using a camera is advantaged in that multiple particle positions can be recorded simultaneously, the main disadvantage is the speed that data can be obtained. The latest CCD/CMOS cameras are only able to record data in the order of Kilo Hertz, whereas a QPD can record in the order of ~100 kHz. A QPD consists of a photo diode with light sensitive quadrants. Light from either the trapping laser or a second low power probe laser is focused on the QPD using the condensing lens of the microscope (back focal plane). As the particle moves in the trap laser light is deflected, creating a voltage change from the output of the QPD. By moving the particle a set distance either using a piezo electric stage or moving the trap, the calibration constant can be calculated. The stage moving technique introduces difficulty in that stuck particles cannot always be found. Moving the stage also introduces inaccuracy due to the particle being at a different distance from the cover glass (z position) when calibrating to when a measurement will be performed.

Piezoelectric devices function by applying an electric field to produce a mechanical deformation [43]. As large voltages are required to expand the piezoelectric material a

small amount, piezoelectric devices can produce very accurate displacements at relatively high forces. An average piezoelectric stage for microscopy is able to provide nanometre resolution to displacements up to 300 microns (for further information on pizioelectric stage technology see the Appendix).

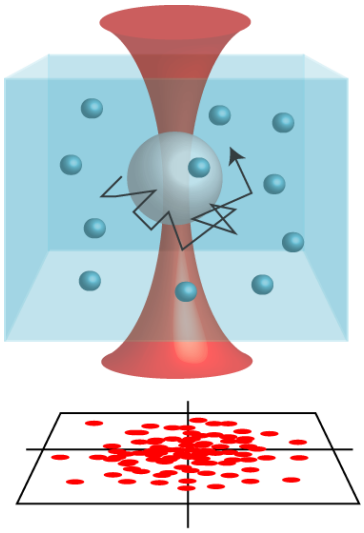

Figure 25: Picture showing a particle optically trapped, undertaking Brownian motion, with an interference pattern displayed on a QPD below. Image sourced from Stephen Keen.

3.6.1 Microrheology Using Optical Tweezers.

Optical tweezers have the ability to be used in both passive and active microrheology [2]. A trapped particle still exhibits thermal motion within the optical trap with large displacements suppressed, enabling the use of passive microrheology at time lags shorter than the saturation frequency. This is accomplished by using particle tracking analysis and/or QPD data to extract the rheological properties. At longer time lags the effect of the trap can be seen in the MSD plot, as a plateau indicating the effect of the trap, as shown in figure (18). Using a trap to perform particle tracking microrheology, as previously described, enables placing a particle(s) in a precise position. In a highly heterogeneous medium this has the added advantage of taking measurements in different positions through the material. Active microrheology is a micrheology technique that involves using an external force on the micro sized particles, as opposed to using thermal energy from the environment; this can be done using magnetic tweezers or optical tweezers[2]. Active microrheology using optical tweezers is commonly performed by either oscillating the piezoelectric stage or oscillating the trap. Active microrheology has the ability to probe the rheological properties to much higher time lags and forces than passive techniques as it is not limited to thermal energy, but

was not studied here other than in using a drag method, described in due course to calibrate the trap strength[2].

4 Optical Tweezers Trap Stiffness Calibration

The force (pN's – 100pN's) that optical tweezers exert on dielectric particles makes them the ideal force transducer to probe the mechanics of single molecules [44]. To apply a force to the molecule of interest the molecule must be held at either end, this is achieved by specifically coating a particle so that the molecule attaches, in effect creating molecular handles. Once the molecule is attached to a particle at either of its ends, the particles can be trapped and pulled apart to stretch the molecule. To know how much force is exerted on the trapped particle during a stretching experiment one must first calculate the trap stiffness. This is done experimentally as the many variables needed to theoretically evaluate the trap stiffness are too difficult to measure in practice. Particles optically trapped exhibit Brownian motion with low period oscillations supressed. The motion is that of an over damped harmonic oscillator in a harmonic potential. For displacements smaller than a particle radius the trapping force can be modelled as a Hookean spring [36]:

$$f = -\kappa x \tag{36}$$

Where κ is the spring constant, f is the trapping force, and x is the distance from the centre of the trap to the centre of the trapped particle. By calibrating the trap strength to obtain κ one can calculate the force being exerted on a trapped particle.

4.1.1 Drag Method

A simple method to apply a known force to a micron sized particle is by dragging it through a viscous medium at a known velocity. To validate this method one must ensure that the Reynolds number, defined as: the ratio of inertial forces to viscous force, is small. On a micron length scale the Reynolds number is very low ($10^{-9} - 10^{-4}$), indicating that viscous forces dominate over inertia [21]. Since Reynolds number is low Stokes theorem can be used to describe the force necessary to displace a sphere of radius, a, through an unbound, viscous fluid of viscosity, η, at a velocity, v:

$$f = \gamma_0 v \tag{37}$$

Where, γ_0, is the viscous drag coefficient for a sphere in an unbound fluid defined as:

$$\gamma_0 = 6\pi\eta a \tag{38}$$

Here, a, represents the radius of the sphere.

Finally giving:

$$\kappa x = 6\pi\eta a v \tag{39}$$

[37, 45]. To provide a flow in an optical tweezers experiment one can oscillate the stage with the particle held in an optical trap. Measuring how far the particle deviates from the centre of the trap, when the stage is oscillated, allows calibration of the trap strength (figure 26).

The drag method is computationally simple, although the experimental method to oscillate the stage is much more difficult and time consuming to implement than other methods. Another much more fundamental limit is that it only works in purely viscous homogenous fluids, which many samples of interest are not. This limits the method severely so it is not currently often used.

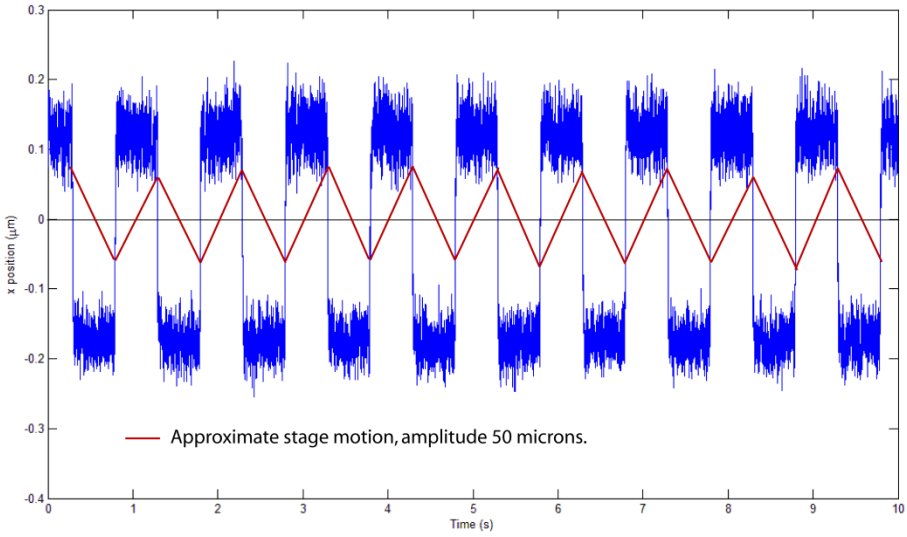

Figure 26: Displacements of a trapped particle as an oscillatory flow is applied by oscillating the stage. Data recorded at 80 kHz for 10 seconds.

4.1.2 VARIANCE METHOD

The effect of the trap on the MSD of a trapped particle can be observed in figure (27), it can be seen that in the region where the effect of the trap has saturated the motion of the particle, the MSD plateaus. The displacement that this corresponds to is directly related to the strength of the laser. In the plateau region the average amount of thermal energy the particle has is in equilibrium with the average energy the trap exerts on the particle, analogous to a mass on a spring. From this one is able to calculate the trap strength using only the thermal energy that the environment supplies.

The average energy of the Brownian motion of a trapped particle, from thermal energy in the environment, in one dimension is: $\frac{1}{2}k_BT$, from the equipartition theorem. The average energy the trap exerts on the particle is related to Hookes law, analogous to a classical spring and mass, is related by: $\frac{1}{2}\kappa < x^2 >$. Once the varience, $< x^2 >$, is calculated one can rearrange the two energy equations to solve for the trap stiffness [45, 46]:

$$\kappa = \frac{k_BT}{< x^2 >} \tag{40}$$

This method is not computationally intensive, although is susceptible to low frequency noise and drift. A simple method to overcome problems related to drift is to look at the Allan variance (as described on page 41) to find the optimum time length to record data. This method is advantaged as particle positions can be measured using a camera and therefore one is able to calibrate many traps simultaneously. Standalone software to calibrate the trap strength using the variance method can be obtained from [47].

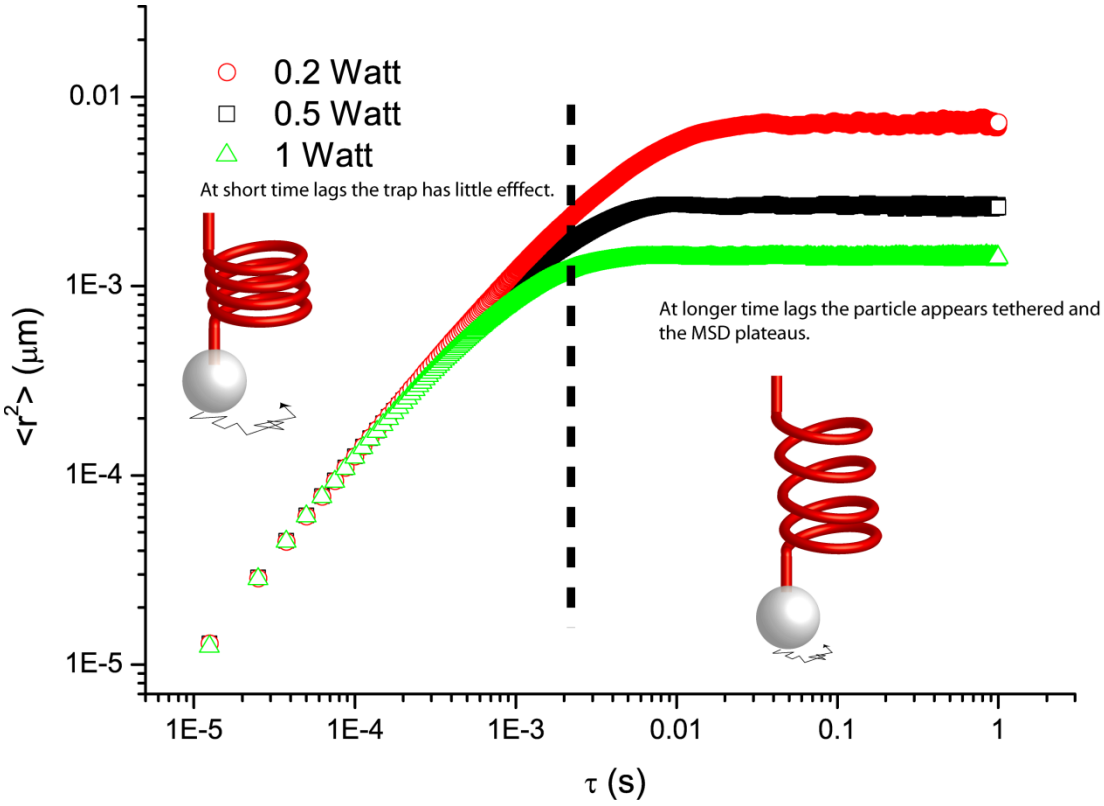

Figure 27: Graph showing the effect of laser power on the MSD of 1.86 micron probe particles.

4.1.3 Power Spectral Density Method

The power spectral density (PSD) method to calibrate the trap strength is reported to be the most reliable method to calibrate optical tweezers [34]. This section follows work by Berg-Sorensen 2004, for more information refer to this reference [34]. This method relies on early work called the Einstein-Ornstein-Uhlenbeck theory of Brownian motion. It predicts a Lorentzian spectrum to a particle in a harmonic potential, such as an optical trap. The Langevin equation for a particle in a trap, in one dimension is [34]:

$$m\ddot{x}(t) + \gamma_0\dot{x}(t) + \kappa x(t) = (2k_BT\gamma_0)^{1/2}n(t) \qquad (41)$$

Here $x(t)$ represents the trajectory of the particle, m its mass, γ_0 the particles friction coefficient, $\kappa x(t)$ is the harmonic force contribution of the trap, and $(2k_BT\gamma_0)^{1/2}n(t)$ a random Gaussian process that represents Brownian forces at an absolute temperature T. The $n(t)$ term for all t and t' is defined by: $\langle\eta(t)\rangle = 0$; $\langle\eta(t)\eta(t')\rangle = \delta(t-t')$ according to the fluctuation dissipation theorem.

Again using Stokes law for a spherical particle:

$$\gamma_0 = 6\pi\eta a \tag{42}$$

Where, η defines the viscosity, and a the particle radius.

As the frequencies measured are lower than where inertial effects come into consideration the terms relating to inertia in the Langevin equation are dropped giving:

$$\dot{x}(t) + 2\pi f_c x(t) = (2D)^{\frac{1}{2}} n(t) \tag{43}$$

Defining the corner frequency as: $f_c = \frac{\kappa}{2\pi\gamma_0}$

the Fourier transform of $x(t)$ and n is now taken, defined as:

$$\tilde{x}_k = \int_{-T_{msr}}^{T_{msr}} \mathrm{d}t e^{i2\pi f_k t}\, x(t) \tag{44}$$

Where f_k is defined as: $f_k = k/T_{msr}$, k as an integer.

the relevant Langevin equation of the Fourier transform can be rewritten as:

$$\tilde{x}_k = \frac{(2D)^{1/2}\tilde{n}_k}{2\pi(f_c - if_k)} \tag{45}$$

The $\dot{x}$ term can be ignored as it has little impact on the final result. It is often referred to as the leakage term.

We can now define the power spectral density as:

$$P_k = |\tilde{x}_k|^2/T_{msr} = \frac{D/2\pi^2 T_{msr}|\tilde{n}_k|^2}{f_c^2 + f_k^2} \tag{46}$$

It is expected that for a $k > 0$ P_k will be a Lorentzian, of the form:

$$P_k = \langle P_k \rangle = \frac{D/(2\pi^2)}{f_c^2 + f_k^2} \tag{47}$$

By fitting the PSD of an optically trapped particle to the above Lorentzian one can obtain the corner frequency and thus the trap stiffness [34]. Programs to accurately calibrate an optical tweezers setup written in MATLAB using the PSD method can be obtained from [48, 49].

5 EXPERIMENTAL METHODS

Having setup and calibrated the microrheological techniques 3 different fluids were then examined; milliQ water, a glycerol water mixture and polyethelene oxide (PEO) solutions. This gave three different environments, namely; low viscosity, high viscosity and viscoelastic, to test the different methods.

Water has a lower viscosity than most biological materials of interest; a low viscosity means that the particle dynamics will be faster for all techniques. This is especially important for light scattering techniques as fast particle dynamics make the correlation function move to shorter lag times, at shorter lag times the signal is noisier, so it is important to test these techniques in low viscosity materials. Water is also the medium of choice for optical trapping as it has a low refractive index, which makes trapping particles easier.

Glycerol, a homogenous, purely viscous fluid was used as it has a high viscosity and is well characterised for many different concentrations. Glycerol and water solutions were made to a concentration of 62 wt%. This value was chosen as it is the highest concentration that can be easily made; due to the high concentration of particles required for DWS measurements. Solutions were made by mixing glycerol, 99.9% from Ajax Laboratory Chemicals and milliQ water using a magnetic flea for approximately 2 hours. Probe particles were then added in concentrations as explained in the following paragraph. The solutions were placed in an ultra-sonic bath for approximately 2 minutes to break up any aggregates that may have formed.

PEO, a viscoelastic polymer solution, was used as it is a well-studied material, homogeneous and is not charged. PEO starts to exhibit viscoelasticity at concentrations higher than the overlap concentration, c^* [5]. The overlap concentration is approximately 0.16 wt% for the 900 KDa PEO samples used in the following experiments [5]. Solutions were made by mixing dry PEO powder (Acros Organics) in milliQ water, and then slowly mixed over approximately a 7day period to help homogenize the solution. Solutions were mixed at a concentration of 2.2wt% and 4wt%, resulting in solutions 14 and 25 times the overlap concentration, to ensure significant viscoelasticity. The solutions were filtered to remove any remaining PEO crystals that would affect the light scattering experiments. Before any measurements are made the PEO and probe particle solution was placed in an ultra-sonic bath for a few minutes to break up any aggregates. This can slightly change the viscoelastic properties of the solution, although, as this was done to all the samples, the different

methods should produce concurrent results. The mesh size of PEO at 2.2 and 4 wt% has been calculated to be a few nanometres [5]. As there are little surface effects between the particles and solution, the solution is homogenous on the length scale smaller than the particle size, and then the bulk rheology should be equivalent to the single particle microrheology. This was an ideal situation to test the 2 point microrheology method in a viscoelastic medium.

DWS measurements require a high bead concentration producing a very turbid solution, this ensures strong multiple scattering for DWS measurements. While Optical tweezers and DLS measurements require that the concentration of particles in the solution is very low. For optical tweezers one must ensure that that there is only one particle present in the imaging plane, any more and there is a chance that one might get sucked into a trap, ruining any results. DLS requires that light be scattered only a single time. For DLS and DWS polystyrene particles are chosen due to their low density and good scattering properties. Silica particles are used for optical tweezers due to the high refractive index of silica, this ensures a strong trapping force.

For the three different materials particle concentrations were held consistent. DLS and DWS solutions were made to concentrations of (10^{-5})% and 1% solid polystyrene particles (Polysciences), respectively. Optical tweezers and MPT solutions were made to concentrations of (10^{-5})% solid silica (Bangs Laboratories) and (1^{-4})% solid fluorescence polystyrene particles (Polysciences).

5.1 Experimental Details

5.1.1 Diffusing Wave Spectroscopy

Initially experiments were conducted using a flex99 correlator from correlators.com and a 35 milli-watt Helium Neon laser (Melles Griot). In the quest for shorter lag times and higher accuracy a flex02 correlator (correlator.com) was purchased. Experiments were first run using water to obtain $l^*$of the standard solution, and then repeated on the sample solution containing the same phase volume of scatterers. DWS experiments were typically run for approximately 40 minutes to one hour.

5.1.2 Dynamic Light Scattering

DLS experiments were performed using a 35 milli-watt Helium Neon laser (Melles Griot) and goniometer (Precision Devices) set nominally to measure a 90 degree scattering angle. Measurements were taken for approximately 40 minutes.

5.1.3 Multiple Particle Tracking

An inverted microscope (Nikon Eclipse TE2000-U) on an air damped table (Photon Control) equipped with a mercury fluorescent lamp (X-cite Series 120PC EXFO), a 63x 1.2 NA (Nikon, Plan Apo VC 60x WI) water immersion objective lens, and a range of different cameras: Foculus FO124SC (CCD), prototype DSI-640-mt smartcam (high speed CMOS), Hamamatsu Orca Flash 2.8 (CMOS large detector size and pixel number). Image series were taken for approximately ten seconds; x-y coordinate data extracted using a homebuilt program written using algorithms obtained from: http://physics.georgetown.edu/matlab/. In-house programs to calculate the MSD and Van Hove correlation function were used in combination with a program to extract the rheological information obtained from: http://www.physics.mcgill.ca/~kilfoil/downloads.html.

5.1.4 Optical Tweezers

We used the same microscope as for MPT to tightly focus a 2 watt 1064 nm Nd:YAG laser (spectra physics). Particle displacements were recorded using a 2.5 mW probe laser (Thorlabs S1-FC-675) and QPD (80 kHz), Foculus (42 Hz) and SmartCam (250-500 Hz) for approximately 10 seconds. Flow was introduced by oscillating a piezoelectric multi axis stage (PI P-517.3CD).

5.2 Pollen Tube Growth Medium

As will be explained in due course experiments were carried out with pollen tubes as an example of a biological system in which organelles could be tracked (as opposed to having to add particles). The pollen tubes were studied using a germination medium made as described by Brewbake and Kwack [50]:

0.01g H_3BO_3

0.03g $Ca\ Cl_2 \cdot 2H_2O$

0.02g $MgSo_4 \cdot 7H_2O$

0.01g KNO_3

The above dry chemicals were added to 50ml of milliQ water. The method used differs slightly from the Brewbake method as $Ca\ (NO_3)_2 \cdot 4H_2O$ was replaced with $Ca\ Cl_2 \cdot 2H_2O$ due to the unavailability of calcium nitrate, this had no noticeable detrimental effects on the growth of pollen tubes. Finally this solution was mixed 1:1 with 20% sucrose solution to make a working stock. A sample was prepared by placing ~100 micro litres of germination medium in the well of a single welled microscope slide, flowers were shaken above the well, distributing pollen into the growth medium.

A cover glass was then placed over the well and sealed closed using nail varnish. Samples were left for 30 minutes to an hour, and then viewed under the microscope to see if growth had occurred. Videos were then taken using the Foculus CCD camera with bright field illumination. Image analysis performed using Polyparticle tracking software, described previously, to track organelles in the pollen tube.

6 Results and Discussion

6.1 Comparison of Different Microrheology Methods

Figure (28) shows the three dimensional mean-square displacement as a function of time (log-log plot) for 500nm polystyrene and 1.86 micron silica (normalised to 500nm, optical tweezers data) particles embedded in a 62 wt% glycerol/water mixture and a water solution. The mean-square displacement data shown in figure (28) has an excellent agreement between different methods and also the theoretical result of a slope of one on a log-log mean-square displacement verses time plot. Figure (29) shows the mean-square displacement verses time plot (log-log plot) for 2.2 and 4 wt% PEO with a fit to a sum of power laws with an exponent of ~0.4 and ~0.9, as expected for a polymer solution in the semi-dilute regime and in agreement with previous work. Fitting to a local power law was necessary to help remove noise in the data before calculating the rheological parameters, as having any noise is amplified severely when the second derivative is taken. Figure (29) also shows a good agreement between data obtained using a QPD and DLS for 2.2 wt% PEO and data obtained using MPT and DLS for 4 wt% PEO. Figures (31) and (32) show the frequency dependent viscoelastic properties of the two PEO solutions, these appear in good agreement with previously published work by Dasgupta 2002 [51]. Figure (30) shows data for 2 point analysis of the 4% PEO MPT data, an excellent agreement can be seen to a time lag of 0.2 seconds, after that it deviates significantly from the one point MSD, this is most likely due to drift in the data being amplified by the 2 point analysis as the slope in the non-aligning region is significantly greater than one.

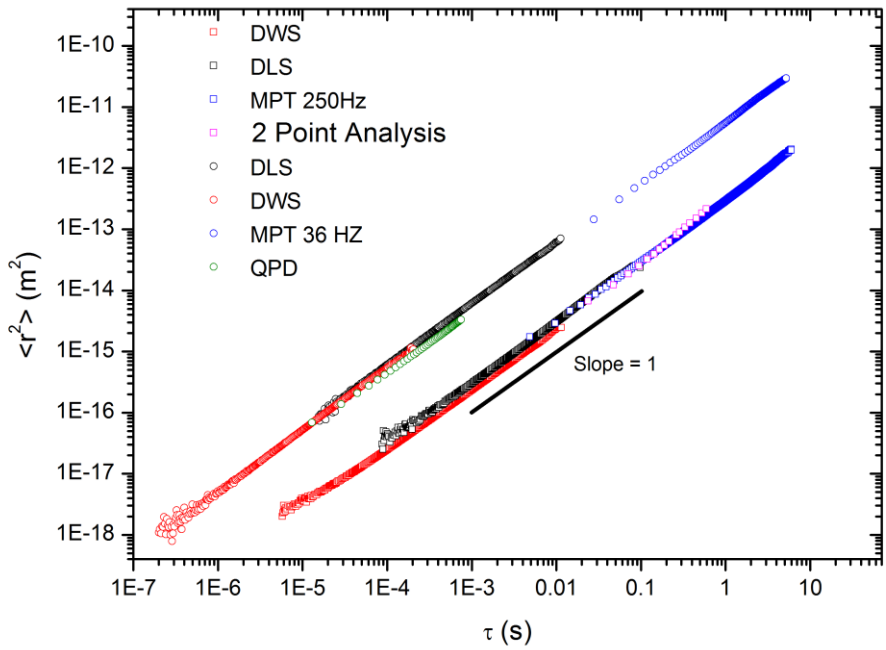

Figure 28: Plot showing the agreement of measurements between multiple techniques in water (open circles) and 62% glycerol water mixture (open squares).

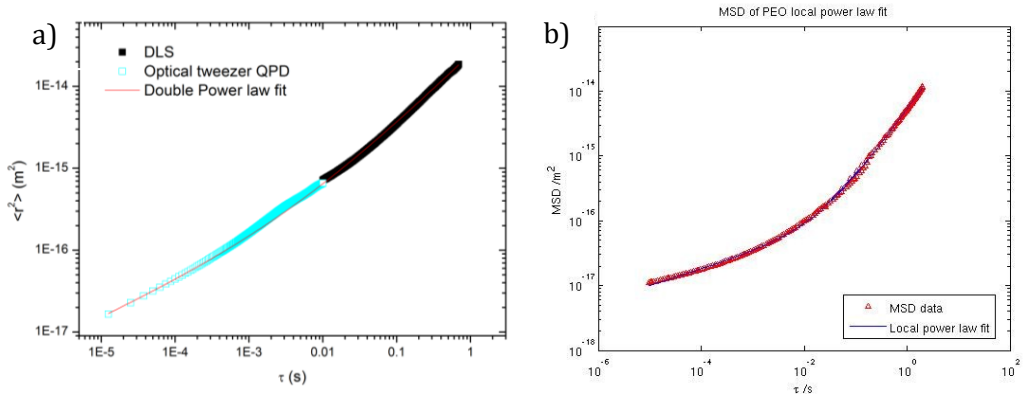

Figure 29: a) MSD for 2.2 wt% 900kDA PEO, a fit to a double power law with exponents of 0.42 and 0.89 shows a good agreement as expected. B) MSD for 4 wt% 900 kDA PEO, a fit to a double power law with exponents of 0.4 and 0.9 shows an excellent agreement.

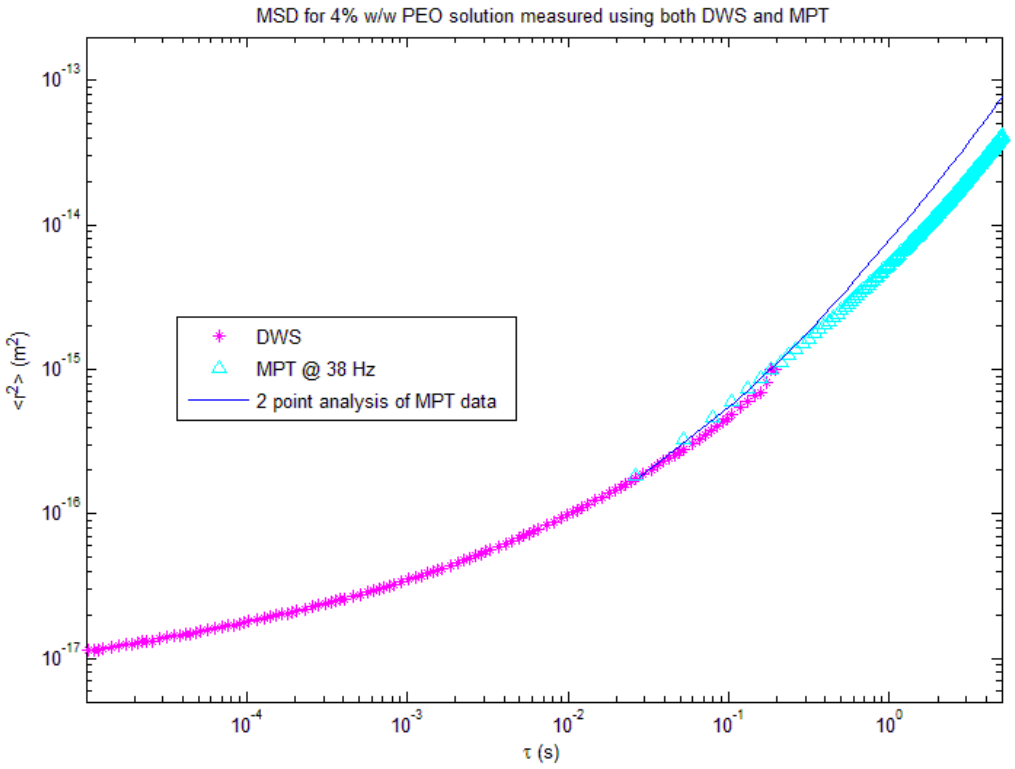

Figure 30: MSD plot for 4 wt% PEO showing an agreement between data obtained using DWS MPT and 2 point analysis.

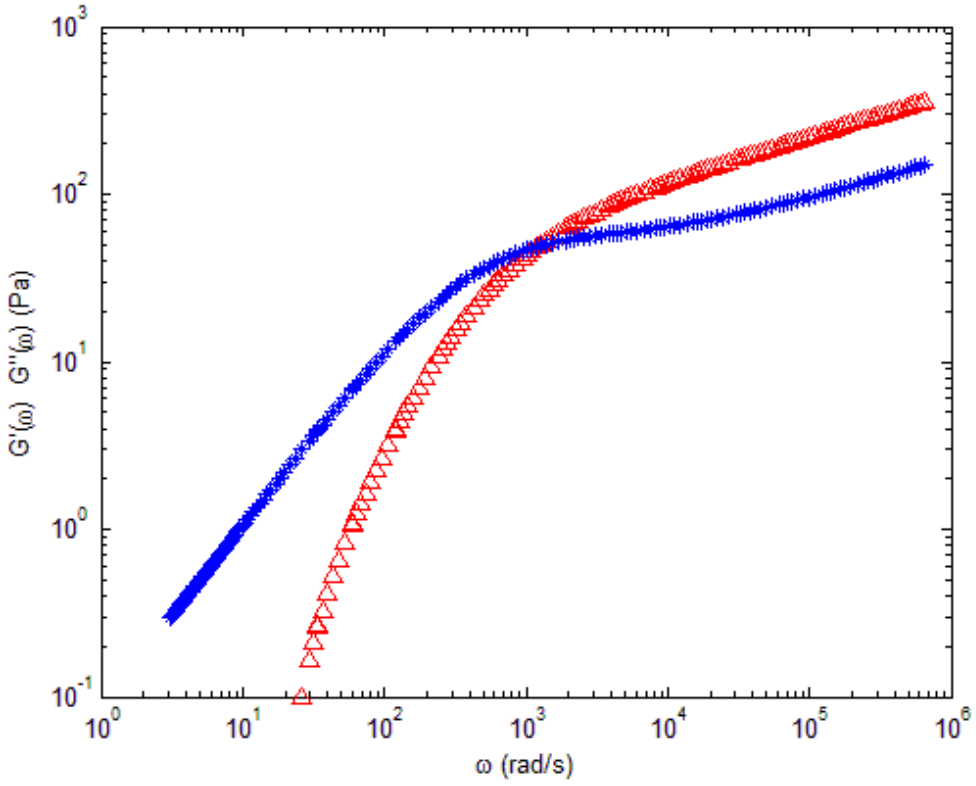

Figure 31: Storage (red) and loss (blue) moduli for a 4 per cent PEO solution.

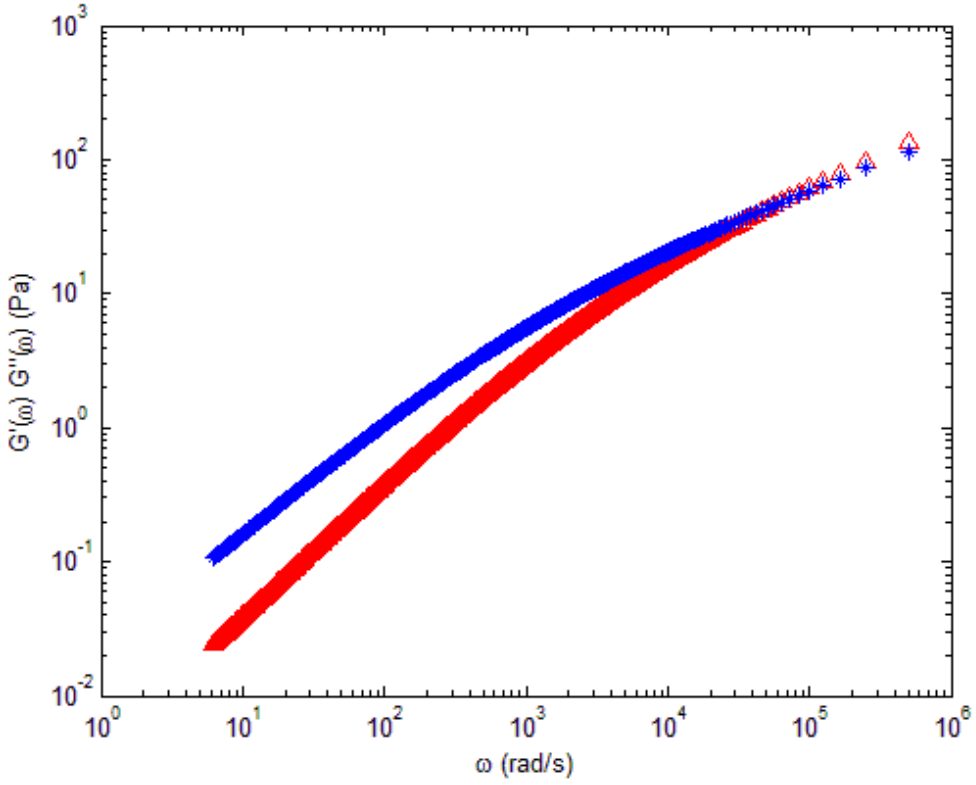

Figure 32: Storage (red) and loss (blue) for 2.2 per cent PEO solution.

6.2 Trap Stiffness Calculation

Figure (33) shows that the different techniques have a strong agreement over a range of trap powers although; the variance method using a camera to obtain the particle displacements displays a deviation from the other methods. This could be from the trap being in a different position on the focal plane. The SLM creates a different interference pattern for traps positioned in different locations on the focal plane; the trap strength is therefore highly dependent on the traps position in the focal plane. It can also be seen that the camera variance method deviates further from the group, in a non-linear fashion, at high laser powers. This could be due to the high trap strength diminishing the particle displacements to levels similar to the resolution of the position acquisition method. This would cause an underestimation of the measured variance, making the trap strength appear unusually high.

The program used to implement the PSD calibration method had the option of correcting for cross-talk between the two channels, as well as correcting for hydrodynamic properties (more information on the program implemented can be found in Tolic-Norrelykke [49]). The main difference can be observed at high laser powers, although the difference is very minor compared to the spread in measured trap strength using different techniques. The data suggests that the trap strength is more difficult to measure in the high laser power regime, revealed by a larger spread of data at high laser powers. It is reported that the PSD method is very accurate at high laser powers, also the PSD method appears accurate through the complete range of laser

strengths. Due to its accuracy and ease of use the PSD method was found to be superior to other methods if a single trap is to be calibrated.

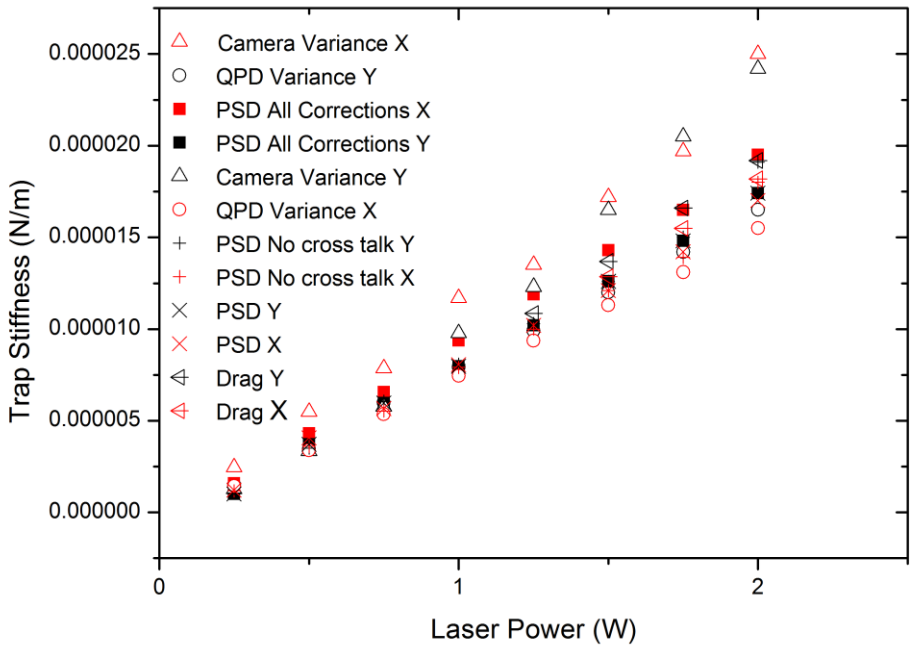

Figure 33: Graph showing trap stiffness measurements for various techniques over a range of laser powers.

7 Tracking Application: Hebe Speciosa Pollen Tubes

7.1 Introduction

Pollen tubes function to transport male gametes from the anther of the donor flower to the female gametes located in the ovule of the receptor plant [52]. Pollen tubes are one of the fastest growing cells, with a growth rate of approximately two to three nanometres per second which corresponds to a speed 50 times faster than the growth of animal nerve cells [53].

Hebe Speciosa, a common ornamental bush that is native to New Zealand, was found to have large vesicles or organelles that could be easily observed using bright field microscopy (figure 34). The mechanics of pollen tube vesicle/organelle transport is generally not well understood, as is shown in a recent review paper by Cai and Cresti [54]. It is theorised that molecular motors drive the motion of the vesicle/organelle along actin filaments through the centre of the pollen tube, while microtubules are present only on the sides of the pollen tube where they interact only when the vesicle/organelle reach the shoulder of the apex. This is shown in figures (35-36)

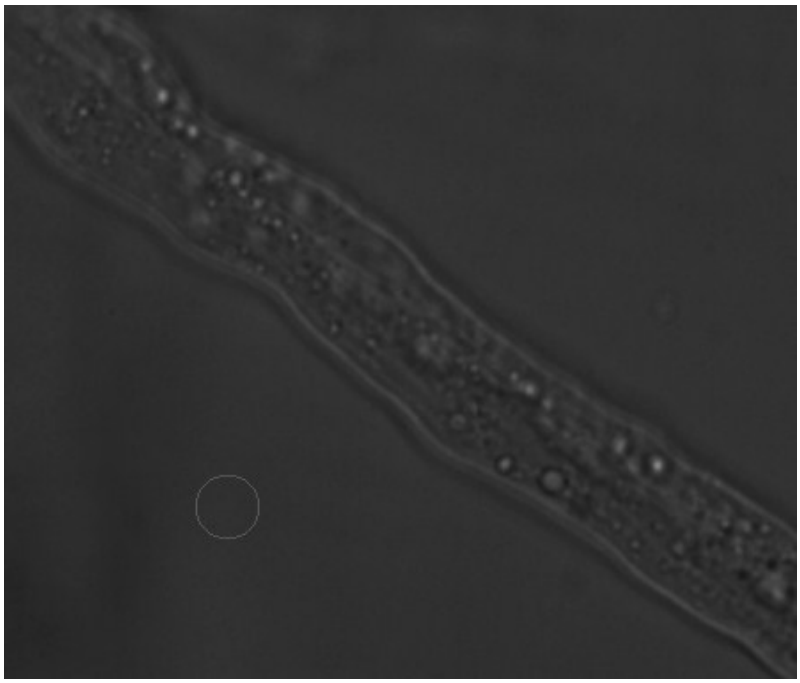

Figure 34: A pollen tube from a Hebe Speciosa.

Biological systems often already contain the probe particles, in this case the probe particles are primarily organelles. The organelles present in pollen tubes are predominately Golgi apparatus, mitochondria and endoplasmic reticulum. Golgi apparatus package and process macromolecules, in the pollen tube they form the vesicles containing pectin and other molecules to grow the pollen tube through exocytosis [54]. Mitochondria are present in pollen tubes primarily to synthesize adenosine triphosphate (ATP), the main form of chemical energy in a cell. Endoplasmic reticulum functions to synthesize proteins, lips and regulate calcium concentration. Calcium concentration is highly important in pollen tubes as it is necessary to bond the pectin molecules to form the networks building the pollen tubes. It has been measured that the oscillatory growth patterns that pollen tubes display is followed by an oscillatory calcium ion concentration pattern of similar periodicity but differing phase [55].

Actin filaments and microtubules are the two filament proteins responsible for the cytoplasmic streaming in pollen tubes, for further information *Mechanics of Motor Proteins and the Cytoskeleton* by Jonathon Howard is a good resource [7].

Polyparticle tracker, which implements the polynomial fit with Gaussian weight algorithm, was chosen to perform the tracking in pollen tubes due to its ability to track both bright and dark particles on a complicated background.

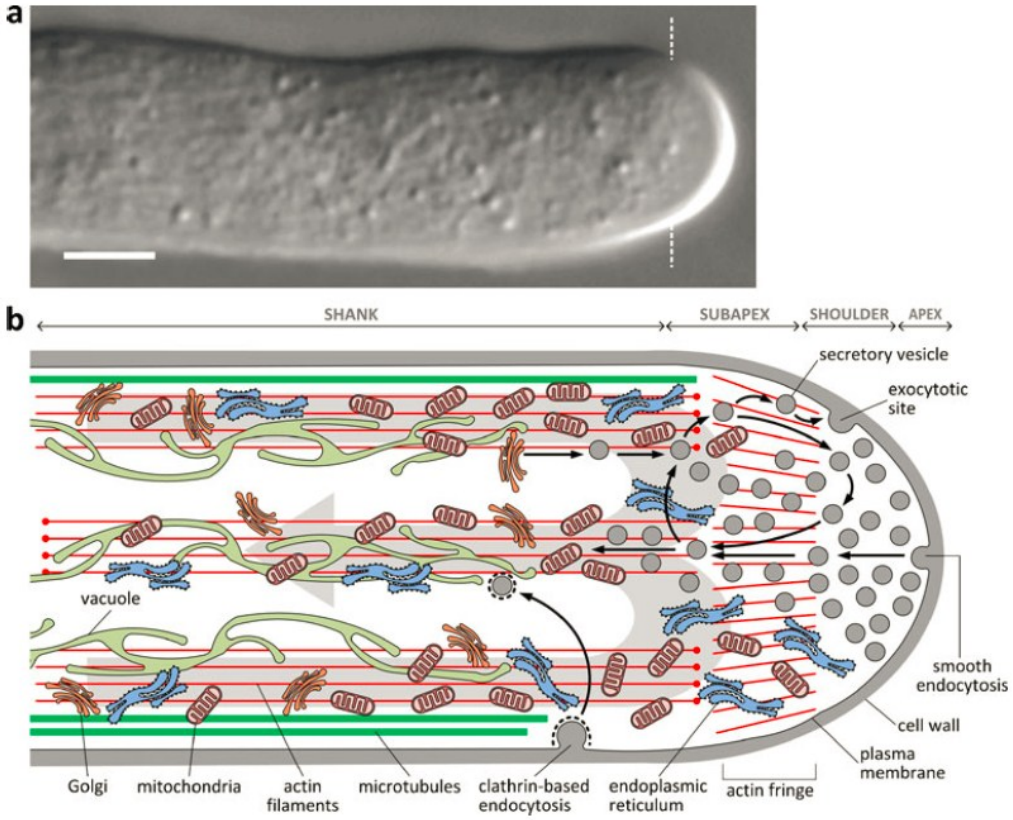

Figure 35: Extract from Cai and Creston 2010, a schematic showing the cytoplasmic streaming of various organelle and vesicles inside a pollen tube with reference to its distance from the tip.

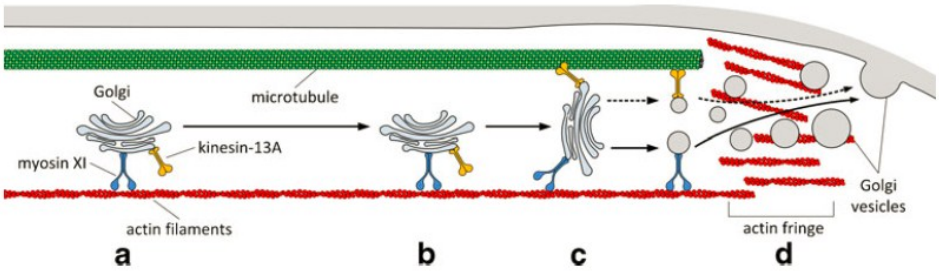

Figure 36: Extract from Cai and Creston 2010 showing a schematic of the theorised mechanics of organelle transport at the apex.

	Cytoskeletal filament	Speed ($\mu m\ s^{-1}$)[a]	Distance covered (μm)	Interaction time (s)	Moving organelles (%)	Frequency of exchange (%)
Mitochondria	MTs	0.17 ± 0.02 ($n = 30$)	5–15	50–60	20	2
	AFs	1.73 ± 0.73 ($n = 45$)	20–25	15–20	85	50
	MTs–AFs	0.53 ± 0.28 ($n = 20$)	n.d.	n.d.	80[b]	10[c]
Golgi vesicles	MTs	0.22 ± 0.05 ($n = 25$)	5–8	40–60	15	10
	AFs	1.78 ± 0.80 ($n = 45$)	12–15	5–10	80	70
	MTs–AFs	0.75 ± 0.49 ($n = 10$)[d]	n.d.	n.d.	75[b]	20[e]

Figure 37: Extract from Romagnoli 2007, table showing the measured speeds of mitochondria and golgi vesicles along microtubules (MT) and actin filaments (AF).

7.2 Results: Pollen Tube Organelle Tracking

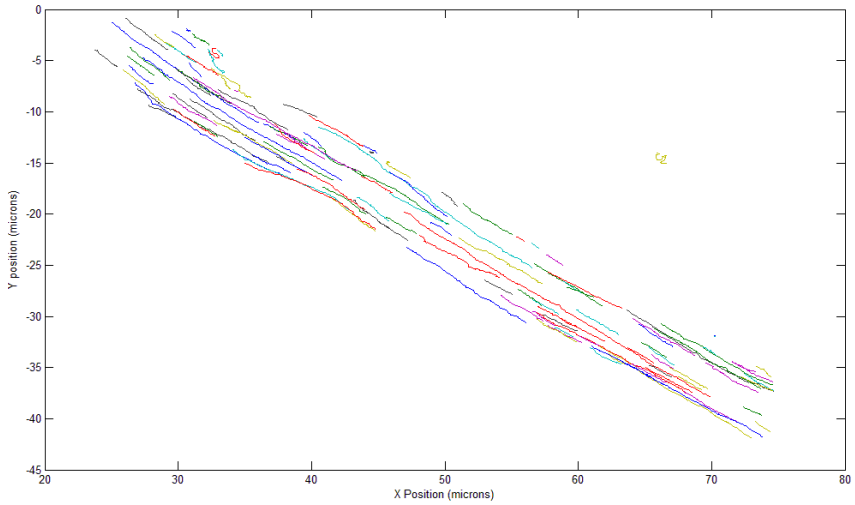

Figure 38: Graph showing the measured vesicle motion in the pollen tube. Each track represents the movement of a vesicle over 10 seconds.

Tracking analysis of organelle motion revealed an average speed of approximately 1.8 microns per second, this is around the expected value, as can be seen from figure (38). A slope of 1.86 was calculated on a log-log MSD verses lag time plot displaying close to purely driven motion throughout the ensemble (purely ballistic motion predicts a log-log MSD verses time slope of 2). A three dimensional Van hove correlation plot (figure 39) shows three distinct populations of organelle motion, one moving in the positive x direction, one in the negative x direction and one with very slow locomotion. The two populations moving quickly in the positive and negative direction are most probably due to the actin/myosin transport system, as the average velocity of these organelles corresponding to the speed measured ex-vivo by Romagnoli et al. 2007 (figure 38) [56]. The population of slow moving organelles are likely to be a mixture of some artefacts the tracking algorithm detected and a very small number of particles that appear, by eye, to travel quickly along the actin filaments then jump onto a microtubule and travel slowly. Due to the low number of particles that appeared to interact with the microtubules it was difficult to extract information about this motion. It was thought that by plotting the Van Hove correlation function in three dimensions discreate spatial steps might be seen, displaying the arm length of the myosin motor proteins, although it appears as though better spatial and temporal resolution is necessary. While particle tracking on pollen tubes has been performed in the past, it is unlikely that tracking has been performed on Hebe Speciosa before. It was an interesting find that Hebe Speciosa's organelles travel at about the same speed through the pollen tube as in-vitro samples.

By using the polyparticle tracking program that implements the polynomial fit with Gaussian weight algorithm one was easily able to track the organelles, even though the background was complicated and the particles going in and out of focus. The data recorded tends to reflect research done by other groups, this preliminary study shows that microrheological techniques can be applied, with ease, to biological samples.

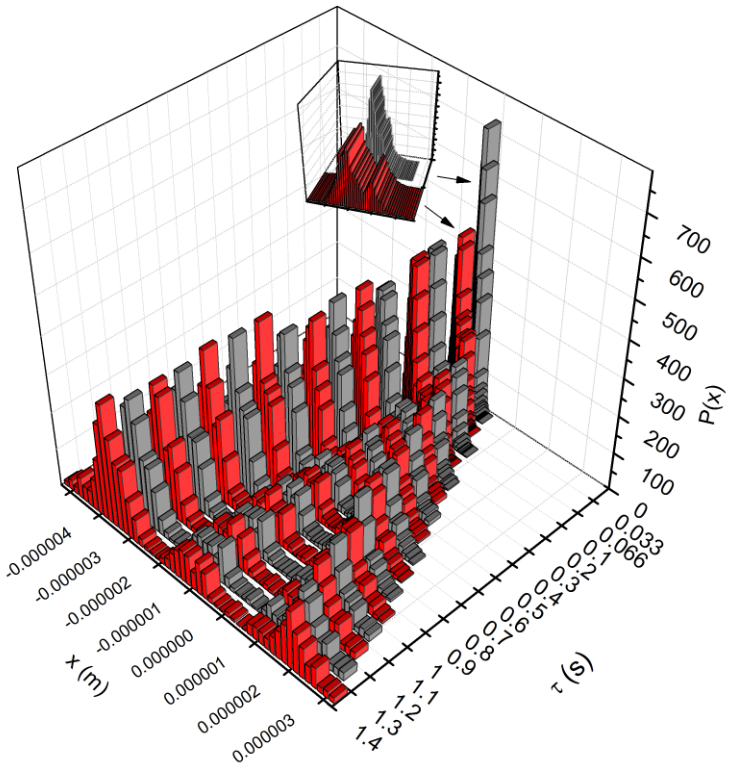

Figure 39: A three dimensional Van Hove correlation function for data obtained from tracking organelle in a Hebe Speciosa pollen tube.

8 CONCLUSIONS

The microrheology techniques refined during the completion of this thesis resulted in the ability to measure the viscoelastic properties of a material over approximately eight orders of magnitude in time $10^{-7} - 10$s (figure 28). The most sensitive technique, DWS, measured particle displacements to nanometre resolution, MPT could measure the largest displacements, on the order of micrometres. Each technique succeeded in measuring the mechanical properties of both a purely viscous and viscoelastic material, reproducing previously published results. These techniques can now be routinely performed on both in-vitro and in-vivo samples with confidence.

Measurements taken to measure the trap strength using different techniques established that at low laser powers all the methods produced very similar results, while at high trap strengths the PSD method produced very accurate results and was also easy to implement. It is recommended that the PSD method be used for trap calibration.

Tracking organelles in pollen tubes using microrheology techniques displayed that these techniques can be used on in-vivo samples. The results measured aligned with previously published results, showing that Hebe Speciosa pollen tubes tend to display similar organelle dynamics to pollen tubes from different species.

9 FURTHER WORK

The final technique to calibrate the optical tweezers would be stretching DNA, as DNA has a well-known force extension plot that you can use it to calibrate optical tweezers. Unfortunately Stretching DNA could not be performed during this thesis, although future work will include this measurement.

It was noticed during the pollen tube experiments that the laser used to trap particles seemed to affect the cytoplasmic streaming of the unresolvable vesicles, causing the pollen tube to grow in a bent fashion. A novel experiment could be conducted from this strange result. Future work to improve the spatial and temporal resolution of the pollen tube data could be carried out, possibly using a QPD for very high resolution, although this seems awkward to implement using the current apparatus.

10 BIBLIOGRAPHY

[1] R. G. Larson, The Structure and Rheology of Complex Fluids, Oxford University Press, New York, 1999.
[2] T. A. Waigh, Reports on Progress in Physics 68 (2005) 685.
[3] M. T. V. M.L. Gardel, D.A. Weitz, Microscale diagnostic techniques, Springer, 2005.
[4] F. C. MacKintosh and C. F. Schmidt, Current Opinion in Colloid & Interface Science 4 (1999) 300.
[5] B. R. Dasgupta, in Department of Physics, Vol. Doctor of Philosophy, Harvard University, Cambridge, Massachusetts, 2004.
[6] T. G. Mason, Rheologica Acta 39 (2000) 371.
[7] J. Howard, Mechanics of motor proteins and the cytoskeleton, Sinauer Associates, Publishers, 2001.
[8] R. Pecora, Dynamic light scattering: applications of photon correlation spectroscopy, Plenum Press, 1985.
[9] P. Zakharov, S. Bhat, P. Schurtenberger, and F. Scheffold, Applied Optics 45 (2006) 1756.
[10] D. A. Weitz and D. J. Pine, in Dynamic Light Scattering: The method and some applications (W. Brown, ed.), Oxford University Press, Oxford, 1993, p. 652.
[11] D. J. P. D. A. Weitz, in Dynamic Light Scattering The Method and Some Applications (W. Brown, ed.), Oxford University Press, New York, 1993, p. 652.
[12] M. Kerker, The scattering of light, and other electromagnetic radiation, Academic Press, 1969.
[13] L. Brunel and H. Dihang, in Xvth International Congress on Rheology - the Society of Rheology 80th Annual Meeting, Pts 1 and 2, Vol. 1027 (A. Co, L. G. Leal, R. H. Colby, and A. J. Giacomin, eds.), 2008, p. 1099.
[14] P. Zakharov, F. Cardinaux, and F. Scheffold, Physical Review E 73 (2006)
[15] J. C. Crocker and B. D. Hoffman, Cell Mechanics 83 (2007) 141.
[16] M. T. Valentine, P. D. Kaplan, D. Thota, J. C. Crocker, T. Gisler, R. K. Prud'homme, M. Beck, and D. A. Weitz, Physical Review E 64 (2001)
[17] Wirtz, Annual Review of Biophysics 38 (2009) 301.
[18] M. T. Valentine, Z. E. Perlman, M. L. Gardel, J. H. Shin, P. Matsudaira, T. J. Mitchison, and D. A. Weitz, Biophysical journal 86 (2004) 4004.
[19] J. C. Crocker, M. T. Valentine, E. R. Weeks, T. Gisler, P. D. Kaplan, A. G. Yodh, and D. A. Weitz, Physical Review Letters 85 (2000) 888.
[20] A. J. Levine and T. C. Lubensky, Physical Review E 65 (2002)
[21] S. Keen, J. Leach, G. Gibson, and M. J. Padgett, Journal of Optics a-Pure and Applied Optics 9 (2007) S264.
[22] S. A. Silburn, C. D. Saunter, J. M. Girkin, and G. D. Love, Review of Scientific Instruments 82 (2011)
[23] T. W. Quan, S. Q. Zeng, and Z. L. Huang, Journal of Biomedical Optics 15 (2010)
[24] I. F. Sbalzarini and P. Koumoutsakos, Journal of Structural Biology 151 (2005) 182.
[25] S. S. Rogers, T. A. Waigh, X. B. Zhao, and J. R. Lu, Physical Biology 4 (2007) 220.
[26] M. K. Cheezum, W. F. Walker, and W. H. Guilford, Biophysical journal 81 (2001) 2378.
[27] J. Gelles, B. J. Schnapp, and M. P. Sheetz, Nature 331 (1988) 450.
[28] T. Savin and P. S. Doyle, Biophysical journal 88 (2005) 623.
[29] T. Savin and P. S. Doyle, Physical Review E 76 (2007)
[30] J. R. Janesick, Scientific charge-coupled devices, SPIE Press, 2001.
[31] S. K. Mendis, S. E. Kemeny, R. C. Gee, B. Pain, C. O. Staller, Q. S. Kim, and E. R. Fossum, Ieee Journal of Solid-State Circuits 32 (1997) 187.
[32] B. C. Carter, G. T. Shubeita, and S. P. Gross, Physical Biology 2 (2005) 60.

[33] F. Czerwinski, A. C. Richardson, and L. B. Oddershede, Optics Express 17 (2009) 13255.
[34] K. Berg-Sorensen and H. Flyvbjerg, Review of Scientific Instruments 75 (2004) 594.
[35] A. Ashkin, Biophysical journal 61 (1992) 569.
[36] S. Keen, in Department of Physics & Astronomy, Vol. PhD, University of Glasgow, Glasgow, 2009.
[37] K. Svoboda and S. M. Block, Annual Review of Biophysics and Biomolecular Structure 23 (1994) 247.
[38] J. E. Molloy and M. J. Padgett, Contemporary Physics 43 (2002) 241.
[39] A. Ashkin, Proceedings of the National Academy of Sciences of the United States of America 94 (1997) 4853.
[40] J. E. Curtis, B. A. Koss, and D. G. Grier, Optics Communications 207 (2002) 169.
[41] D. G. Grier, Nature 424 (2003) 810.
[42] E. R. Dufresne, G. C. Spalding, M. T. Dearing, S. A. Sheets, and D. G. Grier, Review of Scientific Instruments 72 (2001) 1810.
[43] D. A. Skoog, F. J. Holler, and S. R. Crouch, Principles of instrumental analysis, Thomson Brooks/Cole, 2007.
[44] J. van Mameren, E. J. G. Peterman, and G. J. L. Wuite, Nucleic Acids Research 36 (2008) 4381.
[45] R. M. Simmons, J. T. Finer, S. Chu, and J. A. Spudich, Biophysical journal 70 (1996) 1813.
[46] E. L. Florin, A. Pralle, E. H. K. Stelzer, and J. K. H. Horber, Applied Physics a-Materials Science & Processing 66 (1998) S75.
[47] N. Osterman, Computer Physics Communications 181 (2010) 1911.
[48] P. M. Hansen, I. M. Tolic-Norrelykke, H. Flyvbjerg, and K. Berg-Sorensen, Computer Physics Communications 174 (2006) 518.
[49] I. M. Tolic-Norrelykke, K. Berg-Sorensen, and H. Flyvbjerg, Computer Physics Communications 159 (2004) 225.
[50] J. L. Brewbake and B. H. Kwack, American Journal of Botany 50 (1963) 859.
[51] B. R. Dasgupta, S. Y. Tee, J. C. Crocker, B. J. Frisken, and D. A. Weitz, Physical Review E 65 (2002)
[52] J. H. Kroeger, A. Geitmann, and M. Grant, Journal of Theoretical Biology 253 (2008) 363.
[53] S. T. McKenna, J. G. Kunkel, M. Bosch, C. M. Rounds, L. Vidali, L. J. Winship, and P. K. Hepler, The Plant Cell Online 21 (2009) 3026.
[54] G. Cai and M. Cresti, Protoplasma 247 (2010) 131.
[55] E. S. Pierson, D. D. Miller, D. A. Callaham, J. van Aken, G. Hackett, and P. K. Hepler, Developmental Biology 174 (1996) 160.
[56] S. Romagnoli, G. Cai, C. Faleri, E. Yokota, T. Shimmen, and M. Cresti, Plant and Cell Physiology 48 (2007) 345.

11 APPENDIX:

11.1 CAMERA INFORMATION

Camera	Price	Frame rate	Array size quantum efficiency
Hamamatsu Orca flash 2.8	$20,000	45 Hz @ full resolution 540 @ 1920 x 240	1920 x 1440 68% @ 500nm
Foculus FO124S	£1000	<42 Hz	640 x 480
Smartcam (Durham Smart Imaging)	~£16,000 (Prototype)	<500 Hz	128 x 101

11.2 PIEZOELECTRIC STAGE INFORMATION

Stage	Resolution	Travel	Active axis
PI P-517.3CD (PI)	3nm	100 microns	X,Y,Z
Nano-LPS100 Mad City Labs	0.2nm	100 microns	X,Y,Z
Nano-PDQ Mad City Labs	0.1nm	50 microns	X,Y (High speed stage 400Hz)

11.3 CORRELATOR INFORMATION

Correlator	Price	Minimum sample time
Flex 99	$2,000	12.5 ns
Flex 02	$10,000	1.5625 ns